Theory of coherent acoustic phonons in $In_xGa_{1-x}N/GaN$ multiple quantum wells

G. D. Sanders and C. J. Stanton
Department of Physics, University of Florida, Box 118440, Gainesville, Florida 32611-8440

Chang Sub Kim
Department of Physics, Chonnam National University, Kwangju 500-757, Korea

(Received 29 January 2001; revised manuscript received 3 July 2001; published 20 November 2001)

A microscopic theory for the generation and propagation of coherent LA phonons in pseudomorphically strained wurtzite (0001) $In_xGa_{1-x}N/GaN$ multiple quantum well *pin* diodes is presented. The generation of coherent LA phonons is driven by photoexcitation of electron-hole pairs by an ultrafast Gaussian pump laser and is treated theoretically by using the density matrix formalism. We use realistic wurtzite band structures taking valence-band mixing and strain-induced piezoelectric fields into account. In addition, the many-body Coulomb interaction is treated in the screened time-dependent Hartree-Fock approximation. We find that under typical experimental conditions, our microscopic theory can be simplified and mapped onto a loaded-string problem that can be easily solved.

DOI: 10.1103/PhysRevB.64.235316 PACS number(s): 63.10.+a, 63.20.Kr, 63.22.+m

I. INTRODUCTION

In recent years, experiments have shown that optical excitation of electron-hole pairs in semiconductors by ultrafast lasers can coherently excite longitudinal optical phonon modes in semiconductors.[1–10] In uniform bulk semiconductors, since the laser wavelength is much larger than the lattice spacing, the photogenerated carriers are typically excited by the optical pump over spatial areas that are much larger than the lattice unit cell. As a result, the excited carrier populations are generated in a macroscopic state and the carrier density matrix has only a $q \approx 0$ Fourier component. Coupling of the photoexcited carriers to the phonons leads only to coherent optical phonon modes with $q \approx 0$. Since the frequency of the $q \approx 0$ acoustic phonon is zero, coherent acoustic phonons are not excited in bulk semiconductors.

In semiconductor superlattices, even though the laser pump has a wavelength large compared to the lattice spacing, the pump can preferentially generate electron-hole pairs in the wells. The result is to create photoexcited carrier distributions that have the periodicity of the superlattice. Since the density matrix of the photoexcited carrier populations now has a $q \neq 0$ Fourier component, the photoexcited carriers cannot only couple to the optical phonon modes, but they can also generate coherent acoustic phonon modes with a nonzero frequency and wave vector $q \approx 2\pi/L$, where L is the superlattice period. In superlattices, the coherent phonon oscillation of zone-folded acoustic phonons has been observed in AlAs/GaAs superlattices.[9,10] However, the reflection modulation, observed to be on the order of $\Delta R/R \sim 10^{-5}$–10^{-6}, is very small.[10]

Recently, Sun *et al.*[11] reported studies of coherent acoustic phonon oscillations in wurtzite (0001) $In_xGa_{1-x}N/GaN$ multiple quantum well samples with strain induced piezoelectric fields. Owing to the strong piezoelectric fields at the interfaces, huge coherent acoustic phonon oscillations were observed. The oscillations were strong enough to be seen in the transmision (rather than the usual reflectivity) with $\Delta T/T \sim 10^{-2}$–10^{-3}. The oscillation frequency, in the terahertz range, corresponding to the LA phonon frequency with $q \approx 2\pi/L$, varied between samples in accordance with their different superlattice periods L.

In this paper, we formulate a microscopic model for the generation of coherent acoustic phonons in strained wurtzite superlattices via ultrafast laser photoexcitation of real carriers. Whereas in bulk systems the microscopic theory of coherent LO phonons can be mapped onto a forced oscillator model,[6] we show that coherent LA phonon generation in superlattices, under appropriate conditions, can be mapped onto a *loaded string model* that is readily solved for the lattice displacement. Since acoustic phonons are almost the same in the well as in the barrier, to lowest order we can treat the string as being uniform.[12] The forcing term on the string, however, is not uniform since photoexcitation of carriers occurs only in the wells.

Our paper thus provides justification for using a simple, uniform string model with a nonuniform forcing term, rather than a more complicated microscopic theory. In addition, we provide a microscopic expression for the forcing term to use in the simplified string model. The string model provides additional insight into the physics of the coherent LA phonons.

II. MICROSCOPIC THEORY

In this section, we derive the microscopic theory for coherent acoustic phonon generation in superlattices and multiple quantum wells, including the effects of (i) band structure, (ii) strain, (iii) piezoelectric fields, (iv) Coulomb interactions, and (v) laser optical excitation. In Sec. III, we will show how this reduces to a simplified driven uniform string model with a nonuniform forcing term and a microscopic expression for the forcing term.

We model photogeneration of electrons and holes and the subsequant excitation of coherent acoustic phonons in a multiple quantum well (MQW) *pin* diode shown schematically in Fig. 1. The intrinsic active region consists of a left GaN buffer region, several pseudomorphically strained (0001)

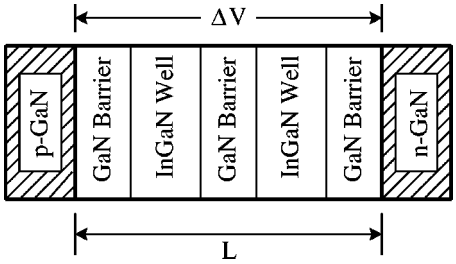

FIG. 1. Schematic diagram of the $In_xGa_{1-x}N$ multiple quantum well diode structure.

$In_xGa_{1-x}N$ quantum wells sandwiched between GaN barriers, and a right GaN buffer region as indicated in the figure. The *P* and *N* regions are assumed to be abruptly terminated *p*- and *n*-doped GaN bulk layers separated by a distance *L* across which a voltage drop, $\Delta V = V_A$, is maintained. Photoexcitation of carriers is achieved by means of an ultrafast laser pulse incident normally along the (0001) growth direction, taken to coincide with the *z* axis.

A. Bulk band structure

In bulk systems, the conduction and valence bands in wurtzite crystals including the effects of strain are treated using effective-mass theory. Near the band edge, the effective mass Hamiltonian for electrons is described by a 2×2 matrix that depends explicitly on electron wave vector **k** and the strain tensor ϵ. The electron Bloch basis states are taken to be

$$|c,1\rangle = |S\uparrow\rangle, \tag{1a}$$

$$|c,2\rangle = |S\downarrow\rangle. \tag{1b}$$

The conduction band Hamiltonian is diagonal and we have (relative to the bottom of the conduction band) (Refs. 13 and 14)

$$H^c_{2\times2}(\mathbf{k},\boldsymbol{\epsilon}) = \left\{ \frac{\hbar^2 k_z^2}{2m_z^*} + \frac{\hbar^2 k_t^2}{2m_{x\text{-}y}^*} + a_{c,z}\epsilon_{z\text{-}z} + a_{c,x\text{-}y}(\epsilon_{x\text{-}x}+\epsilon_{y\text{-}y}) \right\} \mathbf{I}_{2\times2}, \tag{2}$$

where $\mathbf{I}_{2\times2}$ is the identity matrix. The electron effective masses along *z* (taken to be parallel to the *c* axis) and in the *x*-*y* plane are m_z^* and $m_{x\text{-}y}^*$, respectively, $k_t^2 = k_x^2 + k_y^2$, and $\epsilon_{x\text{-}x}$, $\epsilon_{y\text{-}y}$ and $\epsilon_{z\text{-}z}$ are strain tensor components, and $a_{c,z}$ and $a_{c,x\text{-}y}$ are the deformation potentials.

The Hamiltonian for the valence bands is a 6×6 matrix. Following Ref. 15, the Hamiltonian (relative to the top of the valence band) can be block diagonalized into two degenerate 3×3 submatrices if we adopt the Bloch basis states

$$|v,1\rangle = -\frac{\alpha^*}{\sqrt{2}}|(X+iY)\uparrow\rangle + \frac{\alpha}{\sqrt{2}}|(X-iY)\downarrow\rangle, \tag{3a}$$

$$|v,2\rangle = \frac{\beta}{\sqrt{2}}|(X-iY)\uparrow\rangle - \frac{\beta^*}{\sqrt{2}}|(X+iY)\downarrow\rangle, \tag{3b}$$

$$|v,3\rangle = \beta^*|Z\uparrow\rangle + \beta|Z\downarrow\rangle, \tag{3c}$$

$$|v,4\rangle = -\frac{\alpha^*}{\sqrt{2}}|(X+iY)\uparrow\rangle - \frac{\alpha}{\sqrt{2}}|(X-iY)\downarrow\rangle, \tag{3d}$$

$$|v,5\rangle = \frac{\beta}{\sqrt{2}}|(X-iY)\uparrow\rangle + \frac{\beta^*}{\sqrt{2}}|(X+iY)\downarrow\rangle, \tag{3e}$$

$$|v,6\rangle = -\beta^*|Z\uparrow\rangle + \beta|Z\downarrow\rangle. \tag{3f}$$

The phase factors, α and β, are functions of the angle $\phi = \tan^{-1}(k_y/k_x)$ and are given by

$$\alpha(\phi) = \frac{1}{\sqrt{2}}\exp[i(3\pi/4 + 3\phi/2)], \tag{4a}$$

$$\beta(\phi) = \frac{1}{\sqrt{2}}\exp[i(\pi/4 + \phi/2)]. \tag{4b}$$

The block diagonalized Hamiltonian can be written as

$$H^v_{6\times6}(\mathbf{k},\boldsymbol{\epsilon}) = \begin{pmatrix} H^U_{3\times3}(\mathbf{k},\boldsymbol{\epsilon}) & 0 \\ 0 & H^L_{3\times3}(\mathbf{k},\boldsymbol{\epsilon}) \end{pmatrix}, \tag{5}$$

where the upper and lower blocks of the Hamiltonian are

$$H^U_{3\times3}(\mathbf{k},\boldsymbol{\epsilon}) = \begin{pmatrix} F & K_t & -iH_t \\ K_t & G & \Delta - iH_t \\ iH_t & \Delta + iH_t & \lambda \end{pmatrix} \tag{6a}$$

and

$$H^L_{3\times3}(\mathbf{k},\boldsymbol{\epsilon}) = \begin{pmatrix} F & K_t & iH_t \\ K_t & G & \Delta + iH_t \\ -iH_t & \Delta - iH_t & \lambda \end{pmatrix}. \tag{6b}$$

The elements appearing in the 3×3 Hamiltonian matrices are

$$F = \Delta_1 + \Delta_2 + \lambda + \theta, \tag{7a}$$

$$G = \Delta_1 - \Delta_2 + \lambda + \theta, \tag{7b}$$

$$K_t = \frac{\hbar^2}{2m_0}A_5 k_t^2, \tag{7c}$$

$$H_t = \frac{\hbar^2}{2m_0}A_6 k_t k_z, \tag{7d}$$

$$\Delta = \sqrt{2}\Delta_3, \tag{7e}$$

$$\lambda = \frac{\hbar^2}{2m_0}(A_1 k_z^2 + A_2 k_t^2) + D_1\epsilon_{z\text{-}z} + D_2(\epsilon_{x\text{-}x}+\epsilon_{y\text{-}y}), \tag{7f}$$

$$\theta=\frac{\hbar^2}{2m_0}(A_3k_z^2+A_4k_t^2)+D_3\epsilon_{z\text{-}z}+D_4(\epsilon_{x\text{-}x}+\epsilon_{y\text{-}y}). \quad (7g)$$

In Eq. (7), the $A_i's$ are effective-mass parameters, the $D_i's$ are the Bir-Pikus deformation potentials, and the $\Delta's$ are related to the crystal field splitting, Δ_{cr}, and spin-orbit splitting, Δ_{so}, by $\Delta_1=\Delta_{cr}$ and $\Delta_2=\Delta_3=\Delta_{so}/3$. m_0 is the free-electron mass.

B. Quantized carrier states in MQW diodes

In quantum-confined systems such as the *pin* diode shown in Fig. 1, we must modify the bulk Hamiltonian. The finite MQW structure breaks translational symmetry along the z direction but not in the x-y plane. Thus, quantum confinement of carriers in the MQW active region gives rise to a set of two-dimensional subbands. The wave functions in the envelope function approximation are

$$\psi^{\alpha}_{n,\mathbf{k}}(\mathbf{r})=\sum_j \frac{e^{i\mathbf{k}\cdot\boldsymbol{\rho}}}{\sqrt{A}}F^{\alpha}_{n,k,j}(z)|\alpha,j\rangle, \quad (8)$$

where $\alpha=\{c,v\}$ refers to conduction or valence subbands, n is the subband index, $\mathbf{k}=(k_x,k_y,0)=(k,\phi)$ is the two-dimensional wave vector, and j labels the spinor component. For conduction subbands, $(\alpha=c)$ $j=1,2$ while for valence subbands $(\alpha=v)j=1,\ldots,6$. The slowly varying envelope functions $F^{\alpha}_{n,k,j}(z)$ are real and depend only on $k=|\mathbf{k}|$, while the rapidly varying Bloch basis states $|\alpha,j\rangle$ defined in Eqs. (1) and (3) depend on ϕ in the case of valence subbands as given in Eq. (4). The area of the MQW sample in the x-y plane is A, and $\boldsymbol{\rho}=(x,y,0)$ is the projection of $\mathbf{r}$ in the plane.

The envelope functions satisfy a set of effective-mass Schrödinger equations

$$\sum_{j,j'}\{H^{\alpha}_{j,j'}(k)+\delta_{j,j'}[V_{\alpha}(z)-E^{\alpha}_n(k)]\}F^{\alpha}_{n,k,j'}(z)=0, \quad (9)$$

subject to the boundary conditions

$$F^{\alpha}_{n,k,j}(z=0)=F^{\alpha}_{n,k,j}(z=L)=0, \quad (10)$$

where L is again the length of the MQW diode structure (c.f. Fig. 1), $V_{\alpha}(z)$ are the quantum-confinement potentials for conduction and valence electrons, and $E^{\alpha}_n(k)$ are the energy eigenvalues for the nth conduction or valence subband. Note that in the envelope function approximation, the subband energy depends only on the magnitude k of the transverse wave vector and not on the angle ϕ. For the quantum-confined case, the matrix operators $H^{\alpha}_{j,j'}(k)$ depend explicitly on z and are obtained by making the replacement $k_z\rightarrow -i(\partial/\partial z)$ and letting all material parameters be z-dependent operators in the matrices $H^{\alpha}(k,\epsilon)$ given in Eqs. (2) and (5). To ensure the Hermitian property of the Hamiltonian, we make the operator replacements[16]

$$B(z)\frac{\partial^2}{\partial z^2}\rightarrow\frac{\partial}{\partial z}B(z)\frac{\partial}{\partial z}, \quad (11a)$$

and

$$B(z)\frac{\partial}{\partial z}\rightarrow\frac{1}{2}\left[B(z)\frac{\partial}{\partial z}+\frac{\partial}{\partial z}B(z)\right]. \quad (11b)$$

The quantum-confinement potentials $V_c(z)$ and $V_v(z)$ arise from (i) band gap discontinuities between well and barrier regions, (ii) the strain-induced piezoelectric field, and (iii) the time-dependent electric field due to photoexcited electrons and holes. Thus,

$$V_{\alpha}(z,t)=V_{\alpha,\mathrm{gap}}(z)+V_{\mathrm{piezo}}(z)+V_{\mathrm{photo}}(z,t), \quad (12)$$

and the band structure is explicitly time dependent.

Material parameters for InN and GaN used in this work can be found in Table I. For $In_xGa_{1-x}N$ alloys, we interpolate between the GaN and InN values listed in the table.

We obtain electron effective masses by linearly interpolating the reciprocals of the masses as a function of the indium concentration x, i.e., the concentration-dependent effective masses are taken to be

$$\frac{1}{m^*_{x\text{-}y}(x)}=x\left(\frac{1}{m^*_{x\text{-}y}}\right)_{\mathrm{InN}}+(1-x)\left(\frac{1}{m^*_{x\text{-}y}}\right)_{\mathrm{GaN}}, \quad (13a)$$

and

$$\frac{1}{m^*_z(x)}=x\left(\frac{1}{m^*_z}\right)_{\mathrm{InN}}+(1-x)\left(\frac{1}{m^*_z}\right)_{\mathrm{GaN}}. \quad (13b)$$

For the alloy band gap $E_g(x)$, we use an expression incorporating a bowing paremeter:

$$E_g(x)=xE_{g,\mathrm{InN}}+(1-x)E_{g,\mathrm{GaN}}-bx(1-x), \quad (14)$$

where the bowing parameter, $b=1.0$ eV.[18] For all other material parameters, we use linear interpolation in x to obtain values for the alloy. Since we cannot find deformation potentials for InN, we use GaN values by default. In the absence of values of ϵ_{∞} for either GaN or InN, we use linear interpolation in x to obtain ϵ_0 and simply take $\epsilon_{\infty}\approx\epsilon_0$.

If the z dependent band gap in the MQW is $E_g(z)$ as determined from Eq. (14) and the indium concentration profile, and $E_{g,\min}=\min_z[E_g(z)]$ is the minimum band gap in the structure, then the confinement potentials for conduction and valence electrons are defined as

$$V_{c,\mathrm{gap}}(z)=E_{g,\min}+Q_c[E_g(z)-E_{g,\min}], \quad (15a)$$

$$V_{v,\mathrm{gap}}(z)=-(1-Q_c)[E_g(z)-E_{g,\min}], \quad (15b)$$

where the conduction band offset is taken as $Q_c=0.6$.[18] With these definitions for the $V_{\alpha,\mathrm{gap}}(z)$, the zero of the gap confinement potential is placed at the top of the valence-band profile.

The confinement potentials due to the strain-induced piezoelectric field are given by

$$V_{\mathrm{piezo}}(z)=-|e|E^0_z(z), \quad (16)$$

where $|e|$ is the electric charge and $E^0_z(z)$ is the strain-induced piezoelectric field. In a pseudomorphically strained MQW diode, the bulk source and drain (assumed to have

TABLE I. Material parameters for wurtzite InN and GaN. Material parameters for $In_xGa_{1-x}N$ are obtained through interpolation in x as described in the text.

Parameter	InN	GaN
Lattice constants		
a_0(Å)	3.540[a]	3.189[a]
c_0(Å)	3.708[a]	5.185[a]
u_0	0.377[a]	0.376[a]
Direct band gaps (eV)		
E_g	1.95[b]	3.40[b]
Electron effective masses (m_0)		
$m^*_{x\text{-}y}$	0.10[c]	0.18[c]
m^*_z	0.11[c]	0.19[c]
Hole effective mass parameters		
A_1	-9.28[c]	-7.24[c]
A_2	-0.60[c]	-0.51[c]
A_3	8.68[c]	6.73[c]
A_4	-4.34[c]	-3.36[c]
A_5	-4.32[c]	-3.35[c]
A_6	-6.08[c]	-4.72[c]
Hole splitting energies (meV)		
$\Delta_1=\Delta_{cr}$	17.0[c]	22.0[c]
$\Delta_2=\Delta_{s0}/3$	1.0[c]	3.67[c]
Δ_3	1.0[c]	3.67[c]
Electron deformation potentials (eV)		
$a_{c,xy}$		-4.08[d]
$a_{c,z}$		-4.08[d]
Hole deformation potentials (eV)		
D_1		0.7[d]
D_2		2.1[d]
D_3		1.4[d]
D_4		-0.7[d]
Piezoelectric constants (C/m^2)		
e_{31}	-0.57[a]	-0.49[a]
e_{33}	0.97[a]	0.73[a]
Elastic stiffness constants (GPa)		
C_{11}	190[a]	374[a]
C_{12}	104[a]	106[a]
C_{13}	121[a]	70[a]
C_{33}	182[a]	379[a]
C_{44}	10[a]	101[a]
Static dielectric constant		
ε_0	15.3[e]	8.9[f]

[a]Reference 17.
[b]Reference 18.
[c]Reference 19.
[d]Reference 14.
[e]Reference 20.
[f]Reference 21.

identical composition) are unstrained while the in-plane MQW lattice constants adjust to the source and drain values. For a MQW grown along [0001] (the z direction), the z dependent strain is[22]

$$\epsilon_{x\text{-}x}(z)=\epsilon_{y\text{-}y}(z)=\frac{a_0-a(z)}{a(z)}. \tag{17}$$

Here a_0 is the lattice constant in the source and drain and $a(z)$ is the z-dependent lattice constant in the MQW. Minimizing the overall strain energy, we find[22]

$$\epsilon_{z\text{-}z}(z)=-\frac{2C_{13}(z)}{C_{33}(z)}\epsilon_{x\text{-}x}(z), \tag{18}$$

where $C_{13}(z)$ and $C_{33}(z)$ are z-dependent elastic constants.

There are several issues concerning strain that one can worry about. One is the critical well thickness beyond which the strain relaxes. Studies have shown[23] that with 10% indium and 6 nm well width, a 350 kV/cm field is measured, implying that the well is not fully relaxed, which justifies the use of pseudomorphic strain approximation as we do in this paper for wells having 6% indium and thickness near 4 nm. For thick wells, this pseudormorphic strain approximation clearly will begin to break down and a more detailed model will be needed. Interface roughness can also play a role. The roughness will not significantly affect the acoustic phonon modes (see Introduction) but may affect the photogeneration of carriers.[24] For simplicity, we do not consider interface roughness.

The strain-induced polarization directed along z is given by

$$P^0_z(z)=e_{31}(z)[\epsilon_{x\text{-}x}(z)+\epsilon_{y\text{-}y}(z)]+e_{33}(z)\epsilon_{z\text{-}z}(z), \tag{19}$$

where $e_{31}(z)$ and $e_{33}(z)$ are z-dependent piezoelectric constants. The unscreened piezoelectric field in the diode is obtained from the requirement that the electric displacement vanishes.[25] Thus,

$$E^0_z(z)=-\frac{4\pi}{\varepsilon_0(z)}[P^0_z(z)+P_0], \tag{20}$$

where P_0 is a constant polarization induced by externally applied voltages and $\varepsilon_0(z)$ is the position-dependent static dielectric constant. The value of P_0 is obtained from the voltage drop across the diode (of length L) in the unscreened limit, i.e. with no photoexcited carriers. In this limit, the voltage drop between source and drain due to the induced piezoelectric field is just

$$V_A=-\int_0^L dz E^0_z(z), \tag{21}$$

from which P_0 can be determined.

When photoexcited electrons and holes are generated by the laser, then there is an additional time-dependent confinement potential,

$$V_{\text{photo}}(z,t)=-|e|E^{\text{photo}}_z(z,t). \tag{22}$$

This potential is obtained by solving the Poisson equation in the diode for $E_z^{\text{photo}}(z,t)$ subject to the boundary condition

$$V_A = -\int_0^L dz E_z^{\text{total}}(z,t). \tag{23}$$

Here, $E_z^{\text{total}}(z,t)$ is the total electric field and is just the sum of the strain-induced electric field and the field due to photogenerated electrons and holes, i.e.,

$$E_z^{\text{total}}(z,t) = E_z^0(z) + E_z^{\text{photo}}(z,t). \tag{24}$$

Finally, we can write an effective-mass Schrödinger equation for the conduction electron envelope functions in terms of an effective electron potential $V_c^{eff}(z)$:

$$-\frac{\hbar^2}{2}\left\{\frac{\partial}{\partial z}\frac{1}{m_z^*(z)}\frac{\partial}{\partial z}\right\}F_{n,k,j}^c(z) + \{V_c^{eff}(z) - E_n^c(k)\}F_{n,k,j}^c(z) = 0, \tag{25}$$

where the effective electron potential is

$$V_c^{eff}(z) = V_c(z) + \frac{\hbar^2 k^2}{2m_{x\text{-}y}^*(z)} + a_{c,z}(z)\epsilon_{z\text{-}z}(z) + a_{c,x\text{-}y}(z) \times [\epsilon_{x\text{-}x}(z) + \epsilon_{y\text{-}y}(z)]. \tag{26}$$

Similar expressions can be derived for valence electrons. We arrive at a set of coupled ordinary differential equations (ODE's) subject to the two-point boundary value condition of Eq. (10). These are solved for the envelope functions and subband energies.

In practice, we introduce a uniform grid $\{z_i\}$ along the z direction and finite-difference the effective-mass Schrödinger equations to obtain a matrix eigenvalue problem that can be solved using standard matrix eigenvalue routines. The resulting eigenvalues are the subband energies $E_n^\alpha(k)$ and the corresponding eigenvectors are the envelope functions $F_{n,k,j}^\alpha(z_i)$, defined on the finite difference mesh.

C. Second quantized electron Hamiltonians

We next describe the second quantized Hamiltonians for electrons moving freely in the MQW interacting via a screened Coulomb potential. We denote creation and destruction operators for electrons in conduction and valence subbands by $c_{\alpha,n,\mathbf{k}}^\dagger$ and $c_{\alpha,n,\mathbf{k}}$, respectively. The second quantized Hamiltonian for free electrons and holes is simply

$$\mathcal{H}_{e0} = \sum_{\alpha,n,\mathbf{k}} E_n^\alpha(k) c_{\alpha,n,\mathbf{k}}^\dagger c_{\alpha,n,\mathbf{k}}. \tag{27}$$

The Coulomb interaction Hamiltonian is given by

$$\mathcal{H}_{ee} = \frac{1}{2}\sum_{\alpha,n,\mathbf{k}}\sum_{\alpha',n',\mathbf{k}'}\sum_{\boldsymbol{\kappa}\neq 0} \mathcal{V}_{\alpha',n',\mathbf{k}'}^{\alpha,n,\mathbf{k}}(\boldsymbol{\kappa}) \times c_{\alpha,n,\mathbf{k}-\boldsymbol{\kappa}}^\dagger c_{\alpha',n',\mathbf{k}'+\boldsymbol{\kappa}}^\dagger c_{\alpha',n',\mathbf{k}'} c_{\alpha,n,\mathbf{k}}. \tag{28}$$

Equation (28) describes two-body interactions where electrons in states $|\alpha,n,\mathbf{k}\rangle$ and $|\alpha',n',\mathbf{k}'\rangle$ scatter to subband states $|\alpha,n,\mathbf{k}-\boldsymbol{\kappa}\rangle$ and $|\alpha',n',\mathbf{k}'+\boldsymbol{\kappa}\rangle$, respectively. Note that to simplify things, we have neglected terms corresponding to Coulomb-induced interband transitions (the "diagonal approximation") since these are energetically very unfavorable.[26] The electrons thus stay in their original subbands (though they may scatter off from other electrons in different subbands) and exchange crystal momentum $\boldsymbol{\kappa}$. The matrix elements describing the strength of these transitions are given by

$$\mathcal{V}_{\alpha',n',\mathbf{k}'}^{\alpha,n,\mathbf{k}}(\boldsymbol{\kappa}) = \int dz \int dz' V_{|\boldsymbol{\kappa}|}(z-z') \times \sum_j F_{n,|\mathbf{k}-\boldsymbol{\kappa}|,j}^\alpha(z) F_{n,k,j}^\alpha(z) \times \sum_{j'} F_{n',|\mathbf{k}'+\boldsymbol{\kappa}|,j}^{\alpha'}(z') F_{n',k',j'}^{\alpha'}(z'). \tag{29}$$

From Eq. (29), it is apparent that the symmetry relation

$$\mathcal{V}_{\alpha',n',\mathbf{k}'}^{\alpha,n,\mathbf{k}}(\boldsymbol{\kappa}) = \mathcal{V}_{\alpha,n,\mathbf{k}}^{\alpha',n',\mathbf{k}'}(-\boldsymbol{\kappa}) \tag{30}$$

must hold.

The Fourier transform in the x-y plane of the screened Coulomb potential depends only on $\kappa \equiv |\boldsymbol{\kappa}|$ and $|z|$ and is given by

$$V_\kappa(z) = \frac{2\pi e^2}{\epsilon_0 A}\frac{e^{-\kappa|z|}}{\kappa\epsilon_s(\kappa)}. \tag{31}$$

To describe screening, we adopt an effective pseudodynamic dielectric function of the form

$$\frac{1}{\epsilon_s(\kappa)} = \frac{\kappa}{\kappa+\kappa_s}. \tag{32}$$

In the pseudodynamic screening model, we completely neglect screening by the massive holes and treat screening by the lighter conduction electrons in the static screening limit. The screening wave vector κ_s is computed in the two-dimensional (2D) limit. Thus[27]

$$\kappa_s = \frac{2\pi e^2}{\epsilon_0}\frac{\partial N_{2D}}{\partial \mu}, \tag{33}$$

where N_{2D}, the two-dimensional conduction-electron density, is related to an effective chemical potential μ by

$$N_{2D} = \frac{m_{x\text{-}y}^* k_B T}{2\pi\hbar^2}\sum_n \ln\left[1+\exp\left(\frac{E_n^c(0)-\mu}{k_B T}\right)\right]. \tag{34}$$

In Eq. (34), $E_n^c(0)$ is the conduction subband energy evaluated at $k=0$. In our simulation, the value of μ is obtained by requiring that N_{2D}, evaluated using Eq. (34), be equal to the value

$$N_{2D}(t) = \sum_{n,\mathbf{k}} f_n^c(k,t) \tag{35}$$

obtained from the time-dependent conduction-electron distribution functions $f_n^c(k,t)$.

D. Photogeneration of carriers

Electron-hole pairs are created by the pump laser and we treat the electric field of the laser in the semiclassical dipole approximation. In this approximation, the electron-laser interaction Hamiltonian is

$$\mathcal{H}_{eL} = -|e|\mathbf{E}(\mathbf{t}) \cdot \sum_{n,n',\mathbf{k}} [\mathbf{d}_{n,n'}^{c,v}(\mathbf{k}) c_{c,n,\mathbf{k}}^{\dagger} c_{v,n',\mathbf{k}} + \text{H.c.}], \tag{36}$$

where H.c. denotes the Hermitian conjugate of the first term. The laser field is $\mathbf{E}(\mathbf{t})$ and the dipole matrix elements are

$$\mathbf{d}_{n,n'}^{c,v}(\mathbf{k}) = \sum_{j,j'} \mathbf{D}_{j,j'}^{c,v}(\phi) \int dz F_{n,k,j}^{c}(z) F_{n',k,j'}^{v}(z). \tag{37}$$

The vector operator $\mathbf{D}_{j,j'}^{c,v}(\phi)$ is a 2×6 matrix with x, y, and z components. Thus,

$$\mathbf{D}_{j,j'}^{c,v}(\phi) \equiv D_X^{c,v}(\phi)\hat{\mathbf{x}} + D_Y^{c,v}(\phi)\hat{\mathbf{y}} + D_Z^{c,v}(\phi)\hat{\mathbf{z}}, \tag{38}$$

where $\hat{\mathbf{x}}$, $\hat{\mathbf{y}}$, and $\hat{\mathbf{z}}$ are unit vectors and

$$D_X^{c,v}(\phi) = \frac{P_2}{\sqrt{2}E_g} \begin{bmatrix} \alpha & -\beta^* & 0 & \alpha & -\beta^* & 0 \\ -\alpha^* & \beta & 0 & \alpha^* & -\beta & 0 \end{bmatrix}, \tag{39a}$$

$$D_Y^{c,v}(\phi) = \frac{iP_2}{\sqrt{2}E_g} \begin{bmatrix} -\alpha & -\beta^* & 0 & -\alpha & -\beta^* & 0 \\ -\alpha^* & -\beta & 0 & \alpha^* & \beta & 0 \end{bmatrix}, \tag{39b}$$

$$D_Z^{c,v}(\phi) = \frac{P_1}{E_g} \begin{bmatrix} 0 & 0 & -\beta & 0 & 0 & \beta \\ 0 & 0 & -\beta^* & 0 & 0 & -\beta^* \end{bmatrix}. \tag{39c}$$

The 6×2 vector operator $\mathbf{D}_{j',j}^{v,c}(\phi)$ is related to the 2×6 operator $\mathbf{D}_{j,j'}^{c,v}(\phi)$ by

$$\mathbf{D}_{j',j}^{v,c}(\phi) = [\mathbf{D}_{j,j'}^{c,v}(\phi)]^*. \tag{40}$$

In Eq. (39), α and β are the ϕ-dependent phase factors defined in Eq. (4) and the Kane parameters, P_1 and P_2, for wurtzite materials are related to the effective masses and energy gaps by[28]

$$P_1^2 = \frac{\hbar^2}{2m_0}\left(\frac{m_0}{m_z^*} - 1\right)\frac{(E_g+\Delta_1+\Delta_2)(E_g+2\Delta_2) - 2\Delta_3^2}{E_g+2\Delta_2}, \tag{41a}$$

$$P_2^2 = \frac{\hbar^2}{2m_0}\left(\frac{m_0}{m_{x\text{-}y}^*} - 1\right) \times \frac{E_g\{(E_g+\Delta_1+\Delta_2)(E_g+2\Delta_2) - 2\Delta_3^2\}}{(E_g+\Delta_1+\Delta_2)(E_g+\Delta_2) - \Delta_3^2}. \tag{41b}$$

For the semiclassical laser field, we write the real electric field as

$$\mathbf{E}(t) = \frac{1}{2}[\hat{\boldsymbol{\epsilon}}\mathcal{E}(t)e^{i\omega t} + \hat{\boldsymbol{\epsilon}}^*\mathcal{E}(t)e^{-i\omega t}], \tag{42}$$

where ω is the photon frequency, $\hat{\boldsymbol{\epsilon}}$ is a complex unit polarization vector, and $\mathcal{E}(t)$ is the pulse shape envelope function. We assume a Gaussian pulse shape

$$\mathcal{E}(t) = \mathcal{E}_0 \exp\left[-\left(\frac{t-t_0}{\tau\sqrt{\frac{1}{2\ln 2}}}\right)^2\right] \tag{43}$$

centered at $t=t_0$ with an intensity full width at half maximum (FWHM) of τ. The maximum electric field strength, $\mathcal{E}_0$, is related to the pump fluence $\mathcal{F}$ by

$$\mathcal{E}_0 = \sqrt{\frac{16\pi\mathcal{F}}{cn_\omega\tau}}\sqrt{\frac{\ln 2}{\pi}}, \tag{44}$$

where n_ω is the index of refraction at the photon frequency.

For linearly polarized light incident normally on the MQW, the polarization vectors are real and given by either $\hat{\mathbf{x}}$ or $\hat{\mathbf{y}}$. For circularly polarized light, the polarization vectors are complex and given by[29]

$$\hat{\boldsymbol{\epsilon}}_{\pm} = \frac{\hat{\mathbf{x}} \pm i\hat{\mathbf{y}}}{\sqrt{2}}. \tag{45}$$

In Eq. (45), the upper sign refers to left circularly polarized light (positive helicity) and the lower sign refers to right circularly polarized light (negative helicity).

E. Coupling to LA phonons

We treat the acoustic phonons in the MQW as bulklike plane-wave states with wave vector $\mathbf{q}$. Since the system exhibits cylindrical symmetry, only $\mathbf{q}=q\hat{\mathbf{z}}$ longitudinal acoustic phonons are coupled by the electron-phonon interaction. The free LA phonon Hamiltonian can be written as

$$\mathcal{H}_{A0} = \sum_q \hbar\omega_q b_q^{\dagger} b_q. \tag{46}$$

where $b_q^{\dagger}$ and b_q are creation and destruction operators for LA phonons with wave vector $\mathbf{q}=q\hat{\mathbf{z}}$. The wave-vector component q of LA phonons in the MQW is thus defined in an extended-zone scheme where $-\infty<q<\infty$. The phonon dispersion relation is given by a linear relation

$$\omega_q = C_s|q| = \sqrt{\frac{C_{33}}{\rho_0}}|q|, \tag{47}$$

where ρ_0 is the mass density and C_s is just the LA phonon sound speed for propagation parallel to $\hat{\mathbf{z}}$.[12] In computing the LA sound speed in the linear phonon dispersion relation of

Eq. (47), we neglect the z dependence of the material parameters and use bulk GaN values for C_{33} and ρ_0.

The LA phonons in wurtzite MQW's interact with the electrons through deformation potential and screened piezoelectric scattering. The electron–LA phonon interaction in an MQW is governed by the Hamiltonian

$$\mathcal{H}_{eA}=\sum_{\alpha,n,n',\mathbf{k},q}\mathcal{M}^{\alpha}_{n,n'}(k,q)(b_q+b^{\dagger}_{-q})c^{\dagger}_{\alpha,n,\mathbf{k}}c_{\alpha,n',\mathbf{k}}. \tag{48}$$

This Hamiltonian describes the scattering of an electron from subband state $|\alpha,n',\mathbf{k}\rangle$ to subband state $|\alpha,n,\mathbf{k}\rangle$ with either the emission or absorption of an LA phonon. We note that the electron wave vector $\mathbf{k}$ in the x-y plane is conserved in this process since, as noted earlier, the phonon wave vector in the x-y plane is zero.

The interaction matrix elements describing deformation and screened piezoelectric scattering are

$$\mathcal{M}^{\alpha}_{n,n'}(k,q)=\sqrt{\frac{\hbar^2}{2\rho_0(\hbar\omega_q)V}}\left[iq\mathcal{D}^{\alpha}_{n,n'}(k,q)-\frac{|e|e_{33}}{\epsilon_{\infty}\epsilon_s(q)}\mathcal{P}^{\alpha}_{n,n'}(k,q)\right], \tag{49}$$

where V is the crystal volume. The first term in Eq. (49) desribes deformation potential scattering while the second term describes screened piezoelectric scattering.

The relative strengths of the various transitions are determined by form factors for deformation potential and piezoelectric scattering. The form factor for screened piezoelectric scattering is given by

$$\mathcal{P}^{\alpha}_{n,n'}(k,q)=\sum_j\int dz F^{\alpha}_{n,k,j}(z)e^{iqz}F^{\alpha}_{n',k,j}(z), \tag{50}$$

while the form factor for deformation potential scattering is defined to be

$$\mathcal{D}^{\alpha}_{n,n'}(k,q)=\sum_j\Theta^{\alpha}_j\int dz F^{\alpha}_{n,k,j}(z)e^{iqz}F^{\alpha}_{n',k,j}(z). \tag{51}$$

The form factor for deformation potential scattering is similar to the form factor for piezoelectric scattering except that in summing over spinor components j, the terms are weighted by j-dependent deformation potentials Θ^{α}_j that can be represented by the row vectors

$$\Theta^{c}_j=\{a_{c,z},a_{c,z}\}, \tag{52a}$$

$$\Theta^{v}_j=\{D_1+D_3,D_1+D_3,D_1,D_1+D_3,D_1+D_3,D_1\} \tag{52b}$$

for conduction and valence electrons, respectively.

F. Electron density matrices

We define statistical operators in terms of the electron and phonon eigenstates. The electron density matrix is

$$N^{\alpha,\alpha'}_{n,n'}(\mathbf{k},t)\equiv\langle c^{\dagger}_{\alpha,n,\mathbf{k}}(t)c_{\alpha',n',\mathbf{k}}(t)\rangle, \tag{53}$$

where $\langle\ \rangle$ denotes the statistial average of the nonequilibrium state of the system.

The interband components of the density matrix, $N^{c,v}_{n,n'}(\mathbf{k},t)$ and $N^{v,c}_{n',n}(\mathbf{k},t)$, describe the coherence between conduction and valence electrons in subbands n and n' and are related to the optical polarization. The intraband components of the density matrix $N^{\alpha,\alpha}_{n,n'}(\mathbf{k},t)$ describe correlations between different subbands of the same carrier type if $n\neq n'$. If $n=n'$, $N^{\alpha,\alpha}_{n,n}(\mathbf{k},t)\equiv f^{\alpha}_n(\mathbf{k},t)$ is just the carrier distribution function for electrons in the subband state, $\psi^{\alpha}_{n,\mathbf{k}}(\mathbf{r})$, defined in Eq. (8).

G. Coherent phonon amplitude

The coherent phonon amplitude of the qth phonon mode $|q\rangle$ is defined to be[6]

$$D_q(t)\equiv\langle b^{\dagger}_q(t)+b_{-q}(t)\rangle. \tag{54}$$

The coherent phonon amplitude is related to the macroscopic lattice displacement $U(z,t)$ and velocity $V(z,t)$ through the relations

$$U(z,t)=\sum_q\sqrt{\frac{\hbar^2}{2\rho_0(\hbar\omega_q)V}}e^{iqz}D_q(t), \tag{55}$$

$$V(z,t)=\sum_q\sqrt{\frac{\hbar^2}{2\rho_0(\hbar\omega_q)V}}e^{iqz}\frac{\partial D_q(t)}{\partial t}. \tag{56}$$

The coherent phonon amplitude $D_q(t)$ will vanish if there are a definite number of phonons in the mode, i.e., if the phonon oscillator is in one of its energy eigenstates, $|q\rangle$. In this case, there is no macroscopic displacement of the lattice.

The coherent phonon distribution is[6]

$$\mathcal{N}^{coh}_q(t)\equiv\langle b^{\dagger}_q(t)\rangle\langle b_q(t)\rangle \tag{57}$$

and the total phonon distribution $\mathcal{N}_q(t)$ can be separated into coherent and incoherent contributions as follows:

$$\mathcal{N}_q(t)=\langle b_q(t)b^{\dagger}_{-q}(t)\rangle\equiv\mathcal{N}^{coh}_q(t)+\mathcal{N}^{incoh}_q(t). \tag{58}$$

In general, a mode can have a number of both coherent and incoherent phonons, but only the coherent phonons contribute to the macroscopic lattice displacement.

We note that at the beginning of the experiment, there are no coherent phonons present, i.e., $\mathcal{N}^{coh}_q(t)=0$, and the incoherent phonon population is described by a thermal distribution, $\mathcal{N}^{incoh}_q(t)\sim e^{-\hbar\omega_q/k_BT}$.

H. Equations of motion

In this section, we develop equations of motion for the electron density matrices and coherent phonon amplitudes. The electron density matrices obey the general equations of motion

$$\frac{\partial N^{\alpha,\alpha'}_{n,n'}(\mathbf{k},t)}{\partial t}=\left\langle \frac{i}{\hbar}[\mathcal{H},c^{\dagger}_{\alpha,n,\mathbf{k}}c_{\alpha',n',\mathbf{k}}]\right\rangle, \tag{59}$$

where [ ] denotes the commutator and $\langle\ \rangle$ denotes the average over an initial ensemble. The density matrices are defined in the electron picture and initially the valence bands are filled while the conduction bands are empty. We have $f^{c}_{n}(\mathbf{k},t=-\infty)=0$ and $f^{v}_{n}(\mathbf{k},t=-\infty)=1$, which implies

$$N^{\alpha,\alpha'}_{n,n'}(\mathbf{k},t=-\infty)=\delta_{n,n'}\delta_{\alpha,v}\delta_{\alpha',v}\,. \tag{60}$$

The total Hamiltonian $\mathcal{H}$ is the sum of the Hamiltonians described in the previous sections, i.e.,

$$\mathcal{H}=\mathcal{H}_{e0}+\mathcal{H}_{ee}+\mathcal{H}_{eL}+\mathcal{H}_{A0}+\mathcal{H}_{eA}\,. \tag{61}$$

In deriving equations of motion for the density matrices, we make the ansatz that the density matrices depend only on $k=|\mathbf{k}|$. We use the rotating wave approximation (RWA) to factor out the rapid $e^{i\omega t}$ behavior of the interband density matrix elements $N^{c,v}_{n,n'}(k,t)$. In the RWA, we have

$$N^{c,v}_{n,n'}(k,t)\equiv\tilde{N}^{c,v}_{n,n'}(k,t)e^{i\omega t}, \tag{62}$$

where $\tilde{N}^{c,v}_{n,n'}(k,t)$ is a slowly varying envelope function. In addition, we treat the Coulomb interaction in the time-dependent Hartree-Fock approximation by factoring four-operator averages arising from $\mathcal{H}_{eL}$ into appropriate products of two-operator averages as described in Ref. 27.

The resulting equations of motion for the density matrices are

$$\begin{aligned}\frac{\partial N^{c,c}_{n,n'}(k,t)}{\partial t}=&\frac{i}{\hbar}\{\mathcal{E}^{c}_{n}(k)-\mathcal{E}^{c}_{n'}(k)\}N^{c,c}_{n,n'}(k)\\&-i\sum_{m}\{\Omega^{c,v}_{n,m}(k)\tilde{N}^{v,c}_{m,n'}(k)-\tilde{N}^{c,v}_{n,m}(k)\Omega^{v,c}_{n,n'}(k)\}\\&+\frac{i}{\hbar}{\sum_{m}}'\{\Lambda^{c}_{n,m}(k)N^{c,c}_{m,n'}(k)\\&-N^{c,c}_{n,m}(k)\Lambda^{c}_{m,n'}(k)\},\end{aligned} \tag{63a}$$

$$\begin{aligned}\frac{\partial N^{v,v}_{n,n'}(k,t)}{\partial t}=&\frac{i}{\hbar}\{\mathcal{E}^{v}_{n}(k)-\mathcal{E}^{v}_{n'}(k)\}N^{v,v}_{n,n'}(k)\\&-i\sum_{m}\{\Omega^{v,c}_{n,m}(k)\tilde{N}^{c,v}_{m,n'}(k)-\tilde{N}^{v,c}_{n,m}(k)\Omega^{c,v}_{n,n'}(k)\}\\&+\frac{i}{\hbar}{\sum_{m}}'\{\Lambda^{v}_{n,m}(k)N^{v,v}_{m,n'}(k)\\&-N^{v,v}_{n,m}(k)\Lambda^{v}_{m,n'}(k)\},\end{aligned} \tag{63b}$$

$$\begin{aligned}\frac{\partial \tilde{N}^{c,v}_{n,n'}(k,t)}{\partial t}=&\frac{i}{\hbar}\{\mathcal{E}^{c}_{n}(k)-\mathcal{E}^{v}_{n'}(k)-\hbar\omega\}\tilde{N}^{c,v}_{n,n'}(k)\\&-i\sum_{m}\{\Omega^{c,v}_{n,m}(k)N^{v,v}_{m,n'}(k)\\&-N^{c,c}_{n,m}(k)\Omega^{c,v}_{m,n'}(k)\}.\\&+\frac{i}{\hbar}{\sum_{m}}'\{\Lambda^{c}_{n,m}(k)\tilde{N}^{c,v}_{m,n'}(k)\\&-\tilde{N}^{c,v}_{n,m}(k)\Lambda^{v}_{m,n'}(k)\}.\end{aligned} \tag{63c}$$

The equations of motion for $\tilde{N}^{v,c}_{n,n'}(k,t)$ are redundant since $\tilde{N}^{v,c}_{n,n'}(k,t)=[\tilde{N}^{c,v}_{n',n}(k,t)]^{*}$.

The first terms on the right-hand side of Eq. (63) describe the free oscillation of the density matrices in the renormalized single-particle energy bands. The time-dependent single-particle energies are

$$\mathcal{E}^{\alpha}_{n}(k,t)=E^{\alpha}_{n}(k)+\Lambda^{\alpha}_{n,n}(k,t), \tag{64}$$

where $E^{\alpha}_{n}(k)$ are the single-particle subband energies in the absence of conduction electrons and holes and $\Lambda^{\alpha}_{n,n}(k,t)$ describes the time-dependent renormalization of the single-particle subbands.

The renormalization energies $\Lambda^{\alpha}_{n,n}(k,t)$ are the diagonal elements of a generalized renormalization energy matrix (in the subband indices)

$$\Lambda^{\alpha}_{n,n'}(k,t)=\Sigma^{\alpha}_{n,n'}(k,t)+Q^{\alpha}_{n,n'}(k,t). \tag{65}$$

The first term in the renormalization energy matrix (65) is the generalized exchange self-energy matrix arising from the Coulomb interaction and is given by

$$\begin{aligned}\Sigma^{\alpha}_{n,n'}(k,t)\equiv&-\sum_{\mathbf{k}'\neq\mathbf{k}}\mathcal{V}^{\alpha,n,k}_{\alpha,n',k'}(|\mathbf{k}-\mathbf{k}'|)\\&\times[N^{\alpha,\alpha}_{n,n'}(k',t)-\delta_{\alpha,v}\delta_{n,n'}],\end{aligned} \tag{66}$$

where $\mathcal{V}^{\alpha,n,k}_{\alpha,n',k'}(|\mathbf{k}-\mathbf{k}'|)$ are angular averaged Coulomb interaction matrix elements. The second term in Eq. (65) accounts for renormalization due to coupling of carriers to coherent acoustic phonons. We have

$$Q^{\alpha}_{n,n'}(k,t)\equiv\sum_{q}D_{q}(t)\mathcal{M}^{\alpha}_{n,n'}(k,q), \tag{67}$$

where $D_{q}(t)$ is the coherent phonon amplitude and the electron-phonon matrix elements $\mathcal{M}^{\alpha}_{n,n'}(k,q)$ are defined in Eq. (49). The self-energy corrections in Eq. (66) are small, though they can be important in some circumstances.

In computing the angular averaged Coulomb matrix elements in Eq. (66), we assume small momentum transfer $\boldsymbol{\kappa}$ and use the fact that the envelope functions $F^{\alpha}_{n,k,j}(z)$ depend weakly on k to obtain an effective interaction,

$$\mathcal{V}^{\alpha,n,k}_{\alpha',n',k'}(\kappa)\equiv\int dz\int dz' V_\kappa(z-z')\sum_{j,j'}\langle|F^{\alpha}_{n,(k,k'),j}(z)|^2\rangle \times\langle|F^{\alpha'}_{n',(k,k'),j'}(z')|^2\rangle, \tag{68}$$

where, by definition,

$$\langle|F^{\alpha}_{n,(k,k'),j}(z)|^2\rangle\equiv\frac{|F^{\alpha}_{n,k,j}(z)|^2+|F^{\alpha}_{n,k',j}(z)|^2}{2}. \tag{69}$$

The effective Coulomb interaction $\mathcal{V}$ defined in Eq. (68) is an even function of κ and is symmetric in α and k, thus preserving the symmetry relation (30). Preserving this symmetry is essential in order to maintain conservation of carriers in the scattering process.

The second terms in Eq. (63) describe photoexcitation of electron-hole pairs by the pump laser. The system reacts to an effective field that is the sum of the applied field and the dipole field of the electron-hole excitations. This gives rise to a matrix of generalized Rabi frequencies in the subband indices

$$\hbar\Omega^{c,v}_{n,n'}(k)=\frac{\mathcal{E}(t)}{2}d^{c,v}_{n,n'}(k)+\sum_{\mathbf{k}'\neq\mathbf{k}}\mathcal{V}^{c,n,k}_{v,n',k'} \times(|\mathbf{k}-\mathbf{k}'|)\tilde{N}^{c,v}_{n,n'}(k',t), \tag{70}$$

which can be shown to satisfy the symmetry relations

$$\hbar\Omega^{c,v}_{n,n'}(k)=[\hbar\Omega^{v,c}_{n',n}(k)]^*. \tag{71}$$

The Gaussian pump envelope function $\mathcal{E}(t)$ is defined in Eq. (43) and the optical dipole matrix elements

$$d^{c,v}_{n,n'}(k)=[d^{v,c}_{n',n}(k)]^*\equiv\int_{-\pi}^{\pi}d\phi\,\hat{\boldsymbol{\epsilon}}\cdot\mathbf{d}^{c,v}_{n,n'}(\mathbf{k}) \tag{72}$$

are angular averages in the x-y plane of the vector dipole matrices dotted into the polarization vector. From Eq. (37), the ϕ dependence of $\mathbf{d}^{c,v}_{n,n'}(\mathbf{k})$ only appears in $\mathbf{D}^{c,v}_{j,j'}(\phi)$ and we can get the angular averages by setting $\alpha(\phi)=\alpha_{avg}=(1-i)/3\pi$ and $\beta(\phi)=\beta_{avg}=(1+i)/\pi$ in the 2×6 matrices $D^{c,v}_X(\phi)$, $D^{c,v}_Y(\phi)$ and $D^{c,v}_Z(\phi)$ defined in Eq. (39).

The last terms in Eq. (63) are similar in structure to the renormalization corrections in the Hartree-Fock energies but are more complicated due to mixing among subbands and involve the off-diagonal components of $\Lambda^{\alpha}_{n,n'}$. The prime on the summation sign indicates that terms containing factors of $N^{\alpha,\alpha'}_{n,n'}(k)$ are excluded from the sum since these terms have already been incorporated in the renormalized Hartree-Fock energies in Eq. (64).

The coherent phonon amplitudes $D_q(t)$ satisfy the driven harmonic oscillator equations

$$\frac{\partial^2 D_q(t)}{\partial t^2}+\omega_q^2 D_q(t)=-\frac{2\omega_q}{\hbar}\sum_{\alpha,n,n',\mathbf{k}}\mathcal{M}^{\alpha}_{n,n'}(k,q)^* \times\{N^{\alpha,\alpha}_{n,n'}(k,t)-\delta_{\alpha,v}\delta_{n,n'}\}, \tag{73}$$

subject to the initial conditions

$$D_q(t=-\infty)=\frac{\partial D_q(t=-\infty)}{\partial t}=0. \tag{74}$$

The closed set of coupled partial differential equations, (63) and (73), for the carrier density matrices and coherent phonon amplitudes are converted into a set of coupled ODE's by discretizing k and q and solving for $N^{\alpha,\alpha'}_{n,n'}(k_i)$ and $D(q_i)$ for each of the mesh points k_i and q_i. The resulting initial value ODE problem is then solved using a standard adaptive-step-size Runge-Kutta routine.[30]

The phonon distributions do not appear in the coupled set of equations (63) and (73). If necessary, they can be determined from $N^{\alpha,\alpha}_{n,n'}(k)$ and the pair of equations

$$\frac{\partial\mathcal{N}^{coh}_q}{\partial t}=-\frac{2}{\hbar}\mathrm{Im}\sum_{\alpha,n,n',\mathbf{k}}\mathcal{M}^{\alpha}_{n,n'}(k,q)B_q N^{\alpha,\alpha}_{n,n'}(k) \tag{75a}$$

and

$$\frac{\partial B_q}{\partial t}+i\omega_q B_q=-\frac{i}{\hbar}\sum_{\alpha,n,n',\mathbf{k}}\mathcal{M}^{\alpha}_{n,n'}(k,q)^* N^{\alpha,\alpha}_{n,n'}(k). \tag{75b}$$

In Eq. (75b), $B_q(t)\equiv\langle b_q(t)\rangle$ satisfies the initial condition $B_q(t=-\infty)=0$. For the incoherent phonon distribution,

$$\frac{\partial\mathcal{N}^{incoh}_q}{\partial t}=0 \tag{76}$$

so no incoherent phonons are generated and the incoherent phonon population maintains its initial thermal equilibrium distribution.

III. LOADED-STRING MODEL

The microscopic equations are rather daunting and detailed. In this section, we show how they can be simplified (under certain conditions) to a more tractable model, namely, that of a driven uniform string, provided one uses the appropriate driving function, $S(z,t)$, which is nonuniform. The microscopics, including details of the superlattice band structure and photogeneration process are included within the driving function.

In our detailed numerical simulations, we use the full microscopic formalism discussed in the previous sections. However, we gain a lot of insight if we can deal with the lattice displacement $U(z,t)$ directly. If we assume that the acoustic phonon dispersion relation is linear as in Eq. (47), then we find that $U(z,t)$ satisfies the loaded-string equation

$$\frac{\partial^2 U(z,t)}{\partial t^2}-C_s^2\frac{\partial^2 U(z,t)}{\partial z^2}=S(z,t), \tag{77}$$

subject to the initial conditions

$$U(z,t=-\infty)=\frac{\partial U(z,t=-\infty)}{\partial t}=0. \tag{78}$$

The LA sound speed C_s is defined in Eq. (47), and the driving function $S(z,t)$ is given by

$$S(z,t) = -\frac{1}{\hbar}\sum_{\alpha,n,n'}\sum_{\mathbf{k},q}\sqrt{\frac{2\hbar C_s|q|}{\rho_0 V}}\mathcal{M}^{\alpha}_{n',n}(k,q)^* \times\{N^{\alpha,\alpha}_{n,n'}(k,t)-\delta_{\alpha,v}\delta_{n,n'}\}e^{iqz}. \quad (79)$$

One may question whether a linear phonon dispersion relation is valid in a superlattice. For small wave vector q, for which elasticity theory holds, the dispersion relation for LA phonons in a superlattice is linear with a dispersion $\omega = \overline{C_s}q$, where $\overline{C_s}$ is the ''average'' sound speed of LA phonons in the well and barriers.[12] This, in fact, has been experimentally verified in InGaN/GaN superlattice samples studied by Sun *et al.*[11]

Note that coherent acoustic phonon generation in a superlattice is qualitatively different than coherent optical phonon generation in a bulk system where only the $q\approx 0$ optic mode can be excited. As a result, both the amplitude $U(z,t)$ and the Fourier transform of the amplitude $D_q(t)$ for an optic mode in bulk satisfy a forced oscillator equation. For the nonuniform, multiple quantum well case, one can excite acoustic modes with $q\neq 0$. The Fourier transform of the amplitude $D_q(t)$ of a coherent acoustic phonon obeys a forced oscillator equation, but owing to the linear dependence of $\omega(q)$ on q, the amplitude itself, $U(z,t)$, obeys a 1D wave equation with a forcing term $S(z,t)$.

Another important point is that Eq. (77) can be taken to be a *uniform* string with a *nonuniform* forcing function. This is because the speed of sound is approximately the same in both the GaN and $In_xGa_{1-x}N$ layers (a more detailed theory would take into account differences in the sound velocities in each layer). For propagation of acoustic modes one can neglect, to lowest order, the differences between the different layers (this is not true for the optic modes). The nonuniformity of the forcing function $S(z,t)$ results from differences in the absorption (not sound velocity) in the well and barrier layers and is, therefore, z dependent. We thus see from Eq. (77) that understanding coherent acoustic phonons in multiple quantum wells is equivalent to understanding a *uniform* string with an *inhomogeneous* forcing term $S(z,t)$ containing the microscopics.

To simplify Eq. (79), we neglect valence band mixing and assume that the effective masses, sound speeds, and coupling constants are uniform over regions where $S(z,t)\neq 0$, i.e., in regions where carriers are being photogenerated. We also assume that the pump pulses are weak enough so that screening of the piezoelectric interaction can be neglected. Finally, if the pump duration is long enough so that transient effects associated with photogeneration of virtual carriers can be ignored, then the off-diagonal elements of the carrier density matrices in Eq. (79) can be dropped. In this case, the driving function takes the simple form

$$S(z,t)=\sum_{\nu} S_\nu(z,t), \quad (80)$$

where the summation index ν runs over carrier species, i.e., conduction electrons, heavy holes, light holes, and crystal-field split holes.

Equation (80) suggests that each carrier species makes a separate contribution to the driving function. The partial driving functions $S_\nu(z,t)$ are

$$S_\nu(z,t)=\pm\frac{1}{\rho_0}\left\{a_\nu\frac{\partial}{\partial z}+\frac{|e|e_{33}}{\epsilon_\infty}\right\}\rho_\nu(z,t), \quad (81)$$

where the plus sign is used for conduction electrons and the minus sign is used for holes. Here $\rho_\nu(z,t)$ is the photogenerated electron or hole number density, which is real and positive, and ρ_0 is the mass density. We note that the loaded-string equation for the propagation of coherent phonons together with the simplified driving function in Eqs. (80) and (81) have also been independently derived by other authors in the limit $e_{33}=0$.[31]

In Eq. (81), the partial driving function for a given species is obtained by applying a simple operator to the photogenerated carrier density. This operator is a sum of two terms, the first due to deformation potential scattering and the second to piezoelectric scattering. The piezoelectric coupling constant e_{33} is the same for all carrier species, while the deformation potential a_ν depends on the species. For conduction electrons, $a_\nu = a_{c,z}$, for heavy or light holes, $a_\nu = D_1 + D_3$, and for crystal field split holes, $a_\nu = D_1$.

It is interesting to note that Planck's constant does not appear in either the loaded-string equation (77) or in its associated driving function defined in Eqs. (80) and (81). Thus, we find that coherent LA phonon oscillations in MQW's can be viewed as an essentially classical phenomenon, an observation that was made in the context of coherent LO phonon oscillations in bulk semiconductors by Kuznetsov and Stanton in Ref. 6.

The driving function $S(z,t)$ satisfies the sum rule

$$\int_{-\infty}^{\infty} dz S(z,t)=0. \quad (82)$$

This is most easily seen from Eqs. (80) and (81), but it also holds for the general expression in Eq. (79). The significance of the sum rule is readily appreciated. After the pump dies away, the carrier density in Eq. (81), neglecting tunneling between wells, is essentially constant and thus $S(z,t)$ is time independent. In the loaded-string analogy, the integral of the driving function over position is proportional to the average force per unit length on the string. If this integral were nonzero, then the center of mass of the string would undergo a constant acceleration resulting in the buildup of an infinite amount of kinetic energy. Such an alarming result in the context of coherent LA phonons is precluded by the sum rule in Eq. (82).

For a given driving function, the wave equation (77), together with the initial conditions (78), can be solved for the coherent phonon lattice displacement by using the Green's function method.[32] Thus,

$$U(z,t)=\int_{-\infty}^{\infty}dt'\int_{-\infty}^{\infty}dz'G(z-z',t-t')S(z',t'). \quad (83)$$

In our MQW diode model, the substrate is assumed to be infinite and the Green's function in this case is just

$$G(z,t)=\frac{\Theta(t)}{2C_s}\{\Theta(z+C_st)-\Theta(z-C_st)\}, \quad (84)$$

where $\Theta(x)$ is the Heaviside step function.

We note that the loaded-string model described above is not restricted to the special case of an infinite substrate and can be extended to study the generation and propagation of coherent LA phonons in more complicated heterostructures. If the driving function $S(z,t)$ due to photoexcited carriers is localized, then the assumptions leading to Eqs. (80) and (81) need only hold in those regions where $S(z,t)$ in nonvanishing. The wave equation applies to regions where the LA sound speed C_s is constant. Heterostructure, in which the LA sound speed is piecewise constant, have abrupt acoustic impedance mismatches that can be handled by introducing more complicated Green's functions or by using other standard techniques.[32,33] An example of such a problem would be a MQW structure embedded in a free-standing substrate in which coherent LA phonons generated in the MQW could bounce back and forth between two parallel substrate-air interfaces.

TABLE II. Simulation parameters for photogeneration of coherent acoustic phonons in a four well MQW diode under flat band biasing conditions. A schematic of the diode structure is shown in Fig. 1.

MQW diode structure	
Left GaN buffer width (Å)	43.0
Number of wells	4
Well width (Å)	63.0
Indium fraction in well	0.06
GaN barrier width (Å)	43.0
Right GaN buffer width (Å)	43.0
Applied bias	
V_A (V)	-0.261
Lattice temperature	
T (K)	300.0
Pump parameters	
Photon energy (eV)	3.21
Fluence (μJ/cm^2)	160.0
Gaussian FWHM (fs)	180.0
Polarization	Left circular

IV. RESULTS

In this section, we discuss simulations based on our microscopic theory of coherent LA phonon generation in a *pin* diode structure with four periods of $In_xGa_{1-x}N$/GaN MQW's photoexcited by a Gaussian pump normally incident along the (0001) z direction. The parameters for our numerical example are listed in Table II. The MQW dimensions and Gaussian pump parameters were chosen to match those typically encountered in room temperature pump-probe differential transmission measurements of coherent LA phonon oscillations carried out by Sun *et al.*[11] on $In_{0.06}Ga_{0.94}N$/GaN MQW structures having 14 periods.

A. Bulk wurtzite band structure

Bulk wurtzite GaN and InN are direct gap materials with band gaps of 3.4 and 1.95 eV, respectively. The bulk band structure of unstrained wurtzite GaN is shown in Fig. 2. As can be seen from equations (2) and (6), the band structure is anisotropic and depends on k_z, the wave vector along the (0001) z axis, and k_t, the wave vector within the x-y plane perpendicular to the z axis. The effective-mass conduction band is twofold degenerate and has a parabolic dispersion with anisotropic effective masses $m_z^*=0.19$ along the z direction and $m_{x\text{-}y}^*=0.18$ in the x-y plane.

The twofold degenerate valence bands are mixtures of heavy hole (HH), light hole (LH), and crystal-field splitoff hole (CH) character. At the zone center, the off-diagonal components of the 3×3 upper and lower Hamiltonians in Eq. (6) vanish and the valence bands can be labeled according to their pure-state wave functions at $k=0$. For the zone-center HH state, the degenerate wave functions are the basis states $|v,1\rangle$ and $|v,4\rangle$ defined in Eq. (3). For the zone-center LH state, the wave functions are $|v,2\rangle$ and $|v,5\rangle$, and for the CH band the zone-center wave functions are $|v,3\rangle$ and $|v,6\rangle$. The heavy-hole effective masses along z and x-y are $m_z^{HH}=|A_1+A_3|^{-1}=1.96$ and $m_{x\text{-}y}^{HH}=|A_2+A_4-A_5|^{-1}=1.92$ for heavy holes, $m_z^{LH}=m_z^{HH}=1.96$ and $m_{x\text{-}y}^{LH}=|A_2+A_4+A_5|^{-1}=0.14$ for light holes, and $m_z^{CH}=|A_1|^{-1}=0.14$ and $m_{x\text{-}y}^{CH}=|A_2|^{-1}=1.96$ for crystal-field splitoff holes.

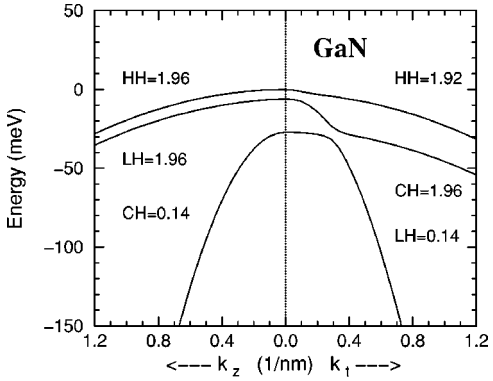

FIG. 2. Bulk GaN valence band structure using effective-mass parameters taken from Table I. The bands are plotted along the (0001) k_z axis and along the transverse k_t axis within the x-y plane. The anisotropic zone-center effective masses for heavy holes (HH), light holes (LH), and crystal-field splitoff holes (CH) are indicated.

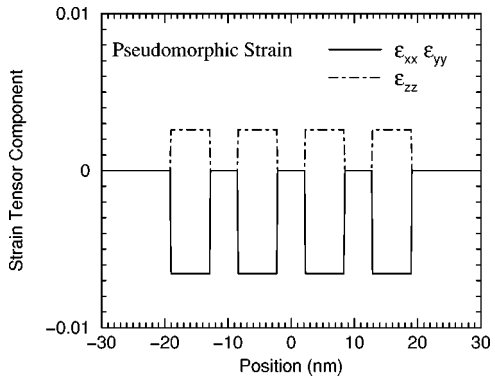

FIG. 3. Strain tensor components for pseudomorphically strained $In_xGa_{1-x}N$ multiple quantum well diode as a function of position. The diode parameters are listed in Table II.

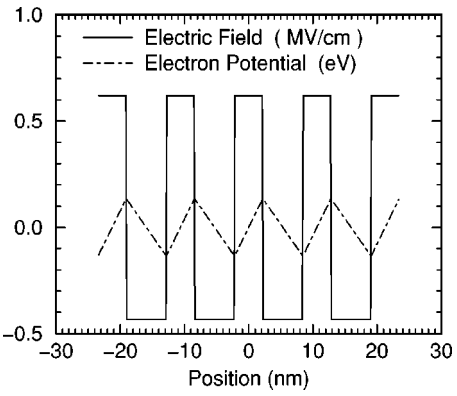

FIG. 4. Electric field and potential for the strain field in Fig. 3. The applied dc bias V_A has been adjusted so flat-band biasing is achieved, i.e., so that the band edges are periodic functions of position. The diode parameters are listed in Table II.

B. Pseudomorphic strain

Bulk GaN and InN have different lattice constants so when an (0001) $In_xGa_{x-1}N$ MQW structure is grown, a significant lattice mismatch occurs between the $In_xGa_{1-x}N$ wells and GaN barriers. For the $In_xGa_{1-x}N$ MQW diode specified in Table II, we assume pseudomorphic strain conditions. In a pseudomorphically strained device, the lattice constant throughout the MQW adjusts to the value of the lattice constant in the bulk N and P substrates in order to minimize the overall strain energy. In our simulated diode, the substrates are $n-$ and $p-$ doped GaN, so the lattice constant throughout the device takes on the GaN value, i.e., $a_0=3.189$ Å. The nonvanishing position-dependent strain tensor components, $\epsilon_{x\text{-}x}$, $\epsilon_{y\text{-}y}$, and $\epsilon_{z\text{-}z}$, for the MQW diode, as computed from Eqs. (17) and (18), are shown in Fig. 3 as a function of *z*. Clearly, the GaN barriers are unstrained since the N and P substrates are composed of GaN and all the strain from the lattice mismatch is accommodated in the $In_{0.06}Ga_{0.94}N$ wells.

C. Built-in piezoelectric field

The presence of strain in the MQW's results in the creation of a strain-induced polarization $P_z^0(z)$, directed along *z* as described by Eq. (19). The strain-induced polarization, in turn, results in a strong bult-in piezoelectric field that can be computed from Eqs. (20) and (21), given the strain field and the dc bias V_A, applied across the diode. The computed strain-induced piezoelectric field $E_z^0(z)$ and the piezoelectric confinement potential $V_{\text{piezo}}(z)$, which result from the strain field in Fig. 3 are shown in Fig. 4. Prior to the application of the pump pulse, we assume that the applied dc bias V_A has been adjusted so that flat-band biasing in the diode is achieved, i.e., V_A is such that the band edges seen in Fig. 4 are periodic functions of position.

Given the piezoelectric field and confinement potentials position-dependent band edges for the MQW can be computed. The conduction and valence band edges for our pseudomorphically strained MQW diode are shown as functions of position in Fig. 5. These are just the confinement potentials, $V_\alpha(z)=V_{\alpha,\text{gap}}(z)+V_{\text{piezo}}(z)$, in the diode prior to photoexcitation. It is clear from Fig. 5 that the confinement of elecrons and holes in the MQW is mostly due to strong built-in piezoelectric fields that result in the triangular confinement potentials seen in each well.

D. Photogeneration of carriers

In our numerical example, we simulate photoexcitation of electrons and holes and the generation and subsequent propagation of coherent LA phonons in the hypothetical MQW diode when a Gaussian pump laser pulse is normally incicent along the *z* axis. As seen in Table II, the Gaussian pump pulse is assumed to be left circularly polarized with a photon energy of 3.21 eV. The pump fluence is taken to be 100.0 μJ/cm^2 and the Gaussian FWHM is taken to be 180.0 fs. The expermient is assumed to take place at room temperature.

In Fig. 6, the computed conduction and valence subband energies are shown as functions of *k* for the $In_xGa_{1-x}N$ diode. At the chosen pump energy of 3.21 eV, electrons from the first two valence subbands are excited into the lowest-lying conduction subband.

The computed densities of photoexcited electrons and holes, neglecting and including Coulomb interaction effects, are shown as functions of position and time in Figs. 7 and 8, respectively, and the total photoexcited electron density per

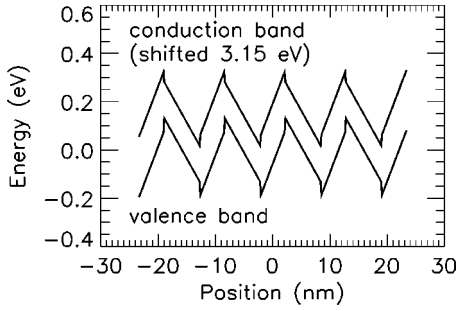

FIG. 5. Conduction- and valence-band edges for pseudomorphically strained $In_xGa_{1-x}N$ multiple quantum well diode as a function of position. The applied dc bias V_A has been adjusted so flat-band biasing is achieved, i.e., so that the band edges are periodic functions of position. The diode parameters are listed in Table II.

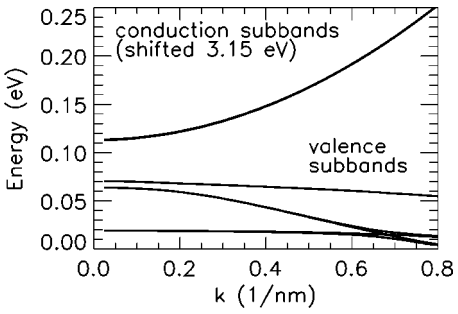

FIG. 6. Conduction and valence subband energies as functions of k for the $In_xGa_{1-x}N$ diode structure described in Table II.

unit area as a function of time is shown in Fig. 9. In Fig. 9 the pulse shape is shown for comparison. We find that including Coulomb effects decreases the total photogenerated carrier density. The electrons and holes screen the built-in piezoelectric field widening the effective band gap. This quantum confined Stark effect acts to suppress the photogeneration of carriers.

E. Generation of coherent phonons

The driving function $S(z,t)$ for the driven string equation (77) is shown in Fig. 10 as a function of position and time.

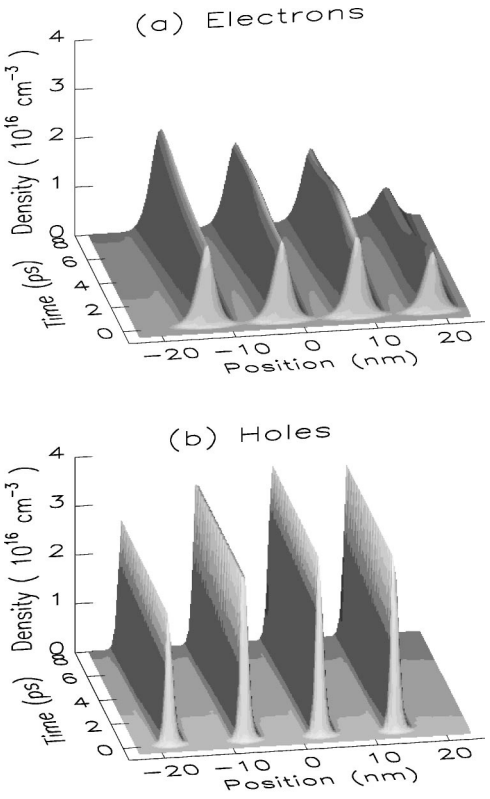

FIG. 7. Density of excited carriers computed in the absence of Coulomb effects for (a) electrons and (b) holes as functions of position for the $In_xGa_{1-x}N$ diode structure and laser pumping parameters shown in Table II.

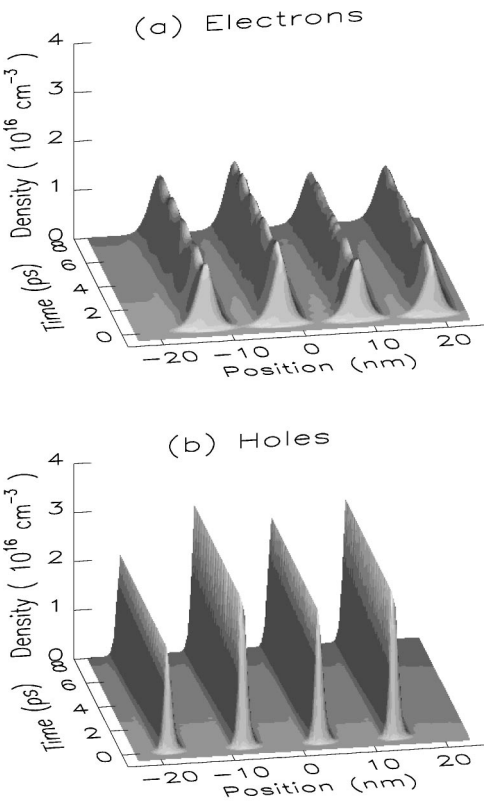

FIG. 8. Density of excited carriers including Coulomb effects for (a) electrons and (b) holes as functions of position for the $In_xGa_{1-x}N$ diode structure and laser pumping parameters taken from Table II.

The driving function has units of acceleration and in Fig. 10, we compute $S(z,t)$ by using the full microscopic formalism of Eq. (79).

For comparison, we also computed the driving function in the simplified loaded-string model of Eqs. (80) and (81) using the carrier densities shown in Fig. 8 to facilitate the comparison. Since the photoexcited holes are predominantly a mixture of heavy and light holes, we use $a_\nu = D_1 + D_3$ in computing hole deformation potential contributions in Eq. (81). The sum over species, ν, then yields the total driving function,

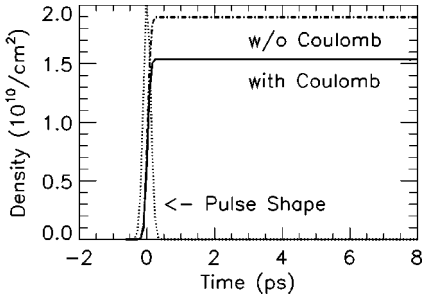

FIG. 9. Total photoexcited electron density with and without Coulomb effects as a function of time for the $In_xGa_{1-x}N$ diode structure and laser pumping parameters listed in Table II. The pulse shape (arbitrary units) is shown for comparison.

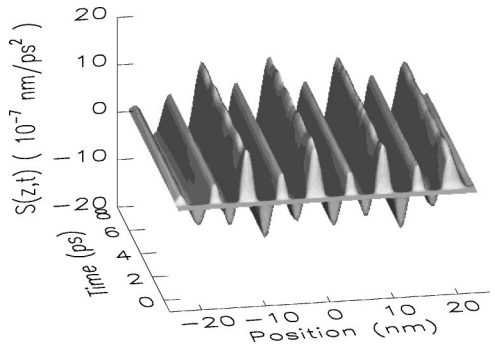

FIG. 10. Driving function $S(z,t)$ for the coherent LA phonon wave equation as a function of position and time for the $In_xGa_{1-x}N$ diode structure and laser pumping parameters in Table II. $S(z,t)$ is computed using the full microscopic expression of Eq. (79).

$$S(z,t)=\frac{1}{\rho_0}\left\{a_{c,z}\frac{\partial}{\partial z}+\frac{|e|e_{33}}{\epsilon_\infty}\right\}\rho_{\rm elec}(z,t)-\frac{1}{\rho_0}\left\{(D_1+D_3)\frac{\partial}{\partial z}+\frac{|e|e_{33}}{\epsilon_\infty}\right\}\rho_{\rm hole}(z,t), \tag{85}$$

where $\rho_{\rm elec}(z,t)$ and $\rho_{\rm hole}(z,t)$ are the total conduction electron and valence hole densities plotted in Fig. 8. The resulting $S(z,t)$ is shown in Fig. 11.

By comparing Figs. 10 and 11, we see that for the diode structure and Gaussian pump used in our simulation the simplified loaded-string model produces essentially the same results as those obtained using the full microscopic formalism.

Acoustic LA phonon generation due to the piezoelectric effect depends on the piezoelectric constant e_{33}, the number of photogenerated electrons and holes, as well as the spatial separation of electron and hole densities brought about by the strong built-in piezoelectric field in the MQW's. From Eq. (85), the piezoelectric contribution to the driving function is given by

$$S_{\rm piezo}(z,t)=\frac{1}{\rho_0}\frac{|e|e_{33}}{\epsilon_\infty}\{\rho_{\rm elec}(z,t)-\rho_{\rm hole}(z,t)\}. \tag{86}$$

In the absence of a built-in piezoelectric field (such as the one found in a square well with infinite barriers), we would

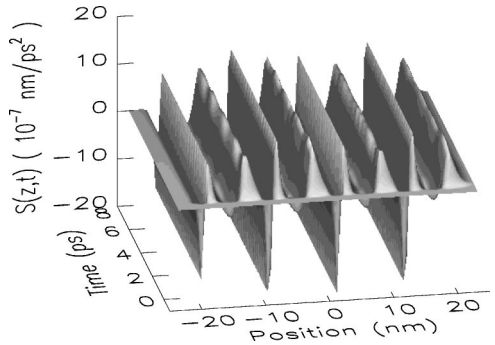

FIG. 11. Driving function $S(z,t)$ in the simplified loaded-string model for the coherent LA phonon wave equation as a function of position and time for the $In_xGa_{1-x}N$ diode structure and laser pumping parameters in Table II.

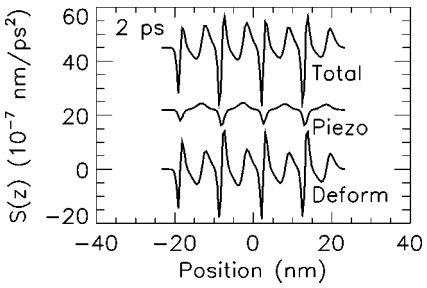

FIG. 12. Driving function $S(z,t)$ in the simplified loaded-string model at $t=2$ ps for the coherent LA phonon wave equation as a function of position for the $In_xGa_{1-x}N$ diode structure and laser pumping parameters in Table II. The total driving function, $S(z,t)$, is the sum of piezoelectric and deformation potential contributions, $S_{\rm piezo}(z,t)$ and $S_{\rm def}(z,t)$.

have $\rho_{\rm elec}(z,t)\approx\rho_{\rm hole}(z,t)$ and hence $S_{\rm piezo}(z,t)\approx 0$, even for relatively large values of e_{33}. The built-in piezoelectric field serves to spatially separate the electrons and holes so that $\rho_{\rm elec}(z,t)\neq\rho_{\rm hole}(z,t)$ and hence $S_{\rm piezo}(z,t)\neq 0$. However, if the built-in piezoelectric field is too strong and the spatial separation of electrons and holes too large, then $\rho_{\rm elec}(z,t)-\rho_{\rm hole}(z,t)\approx 0$. This is because the overlap between the conduction and valence envelope functions enters into the optical dipole matrix elements in Eq. (37). If there is negligible overlap between electron and hole envelope functions due to strong piezoelectric fields then $\mathbf{d}^{cv}_{n,n'}(\mathbf{k})\approx 0$, no electron-hole pairs are photogenerated and once again $S_{\rm piezo}(z,t)\approx 0$.

The deformation potential contribution to the driving function is given by

$$S_{\rm def}(z,t)=\frac{a_{c,z}}{\rho_0}\frac{\partial\rho_{\rm elec}(z,t)}{\partial z}-\frac{(D_1+D_3)}{\rho_0}\frac{\partial\rho_{\rm hole}(z,t)}{\partial z}. \tag{87}$$

From Table I, the conduction electron deformation potential $a_{c,z}$ is roughly twice the valence-hole deformation potential, D_1+D_3. Thus, the two terms in Eq. (87) are of comparable magnitude. The first term, due to conduction electrons, gives rise to a contribution to $S_{\rm def}(z,t)$ which is localized on the right side of each MQW while the second, due to valence holes, gives rise to a contribution that is localized on the left-hand side of each MQW.

In our simulation, we find that piezoelectric and deformation potential contributions to the driving function are comparable. This is seen in Fig. 12 where $S_{\rm piezo}(z)$ and $S_{\rm def}(z)$, along with their sum, are plotted at $t=2$ ps. In this example, we find that $S_{\rm def}(z)$ makes the dominant contribution to $S_(z,t$ as can be seen in Fig. 12.

The macroscopic lattice displacement $U(z,t)$ and velocity field $V(z,t)$ can be obtained from the coherent phonon amplitudes $D_q(t)$ using Eqs. (55) and (56). Alternatively, they can also be obtained from the driving function $S(z,t)$ through the Green's function solution of the driven string equation. In Fig. 13, we plot the macroscopic lattice displacement, $U(z,t)$, and velocity field, $V(z,t)$, for coherent LA phonon modes generated by the driving function shown in Fig. 10.

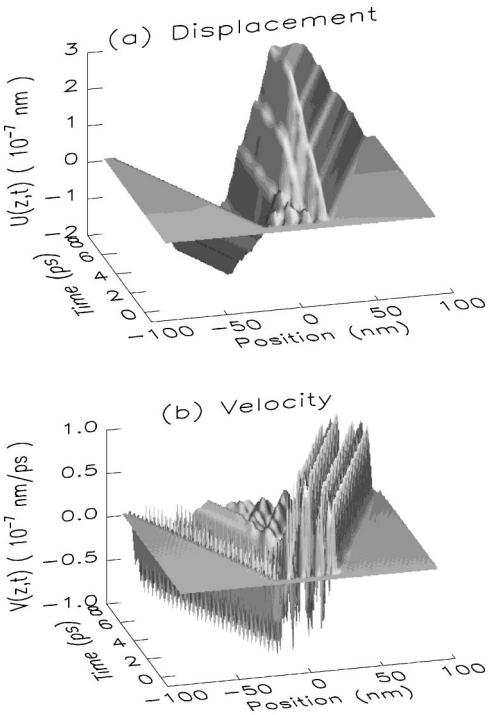

FIG. 13. Lattice displacement $U(z,t)$ and velocity field $V(z,t)$ for coherent LA phonons generated by the driving function shown in Fig. 10.

F. Coherent phonon energy

From the lattice displacement $U(z,t)$, we can obtain the total energy density per unit volume associated with coherent LA phonons,

$$\mathcal{E}_{LA}(z,t)=\mathcal{T}_{LA}(z,t)+\mathcal{V}_{LA}(z,t), \tag{88a}$$

as the sum of a kinetic-energy density term,

$$\mathcal{T}_{LA}(z,t)=\frac{\rho_0(z)}{2}\left(\frac{\partial U(z,t)}{\partial t}\right)^2, \tag{88b}$$

and a potential-energy density term,

$$\mathcal{V}_{LA}(z,t)=\frac{C_{33}(z)}{2}\left(\frac{\partial U(z,t)}{\partial z}\right)^2. \tag{88c}$$

The coherent LA phonon energy per unit area, $E_{LA}(t)$, is obtained by integrating $\mathcal{E}_{LA}(z,t)$ over position z:

$$E_{LA}(t)=\int_{-\infty}^{\infty} dz\,\mathcal{E}_{LA}(z,t). \tag{89}$$

The total energy density $\mathcal{E}_{LA}(z,t)$ for coherent LA phonons as a function of position and time is shown in Fig. 14 and in Fig. 15 the total energy density is plotted as a function of position for equally spaced values of the time ranging from $t=0$ to $t=8$ ps in increments of 2 ps. The curves in Fig. 15 for different times have been offset to avoid overlapping. At short times, the evolution of the total phonon energy density is complicated, but the long time behavior, $t \gtrsim 6$ ps, can be easily understood.

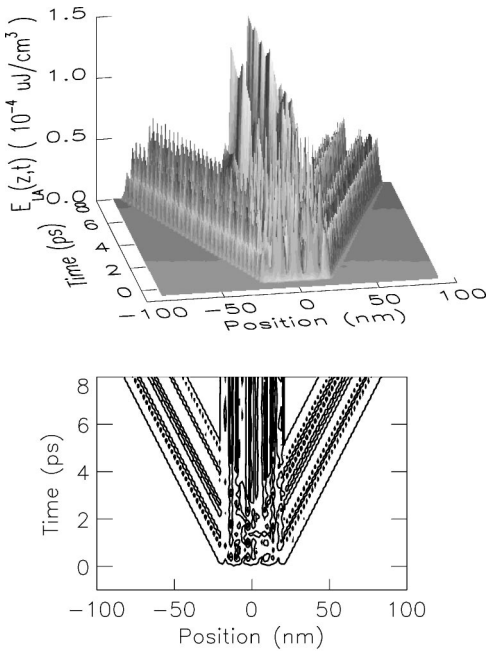

FIG. 14. Total energy density $\mathcal{E}_{LA}(z,t)$ for coherent LA phonons as a function of position and time for the driving function shown in Fig. 10. The total integrated energy density as a function of time is obtained by integrating over position, z

As $t\to\infty$, a localized energy density appears in the MQW region due almost entirely to the potential-energy term in Eq. (88c). This is due to near-steady-state loading by the driving function at long times. Assuming that the driving function $S(z,t)$ is approximately constant at long times, the loaded-string equation (77) can be integrated once in the steady-state limit. We find the steady-state solution

$$\frac{\partial U(z)}{\partial z}\approx -\int_{-\infty}^{z} dz'\frac{S(z')}{C_s^2}, \tag{90}$$

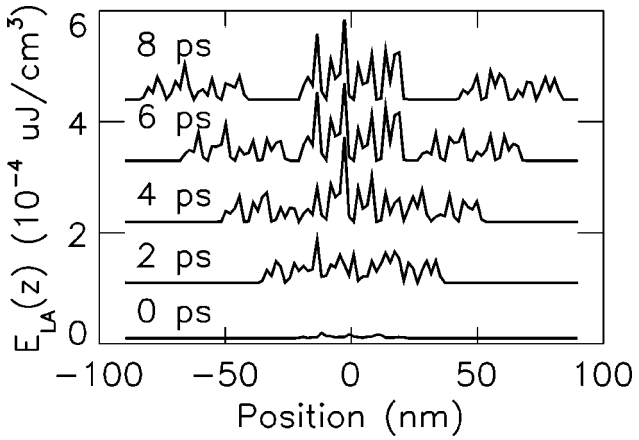

FIG. 15. Total energy density $\mathcal{E}_{LA}(z,t)$ for coherent LA phonons as a function of position for several values of the time t for the driving function shown in Fig. 10. The curves for different times have been offset to avoid overlapping.

from which the long-time behavior of the LA phonon energy density per unit volume in the MQW's,

$$\mathcal{E}^{\infty}_{LA}(z) \approx \frac{C_{33}(z)}{2A}\left(\int_{-\infty}^{z} dz' \frac{S(z')}{C_s^2} \right)^2, \tag{91}$$

can be obtained. The fact that the energy density in Eq. (91) is localized in the MQW's follows directly from the sum rule (82) and is clearly seen in Figs. 14 and 15.

In addition to the localized energy density, which remains behind in the MQW's, two propagating wave trains consisting of four pulses each are seen to exit the MQW region and travel off to infinity at the acoustic phonon sound speed C_s. The distance between the pulses is just the interwell separation distance. In these radiating wave trains, the kinetic and potential energy densities, $\mathcal{T}_{LA}(z,t)$ and $\mathcal{V}_{LA}(z,t)$, are found to be equal as one would expect.

The power spectrum of the coherent LA phonon energy density in q space can be written in terms of the coherent phonon amplitudes $D_q(t)$. The power spectrum for the total coherent LA phonon energy density,

$$\mathcal{E}_{LA}(q,t) = \mathcal{T}_{LA}(q,t) + \mathcal{V}_{LA}(q,t), \tag{92a}$$

is again the sum of a kinetic-energy term,

$$\mathcal{T}_{LA}(q,t) = \frac{1}{2A}\frac{\hbar}{\omega_q}\left| \frac{\partial D_q(t)}{\partial t} \right|^2, \tag{92b}$$

and a potential-energy term,

$$\mathcal{V}_{LA}(q,t) = \frac{1}{2A}\hbar\omega_q |D_q(t)|^2. \tag{92c}$$

The phonon energy density per unit area is obtained by summing the power spectrum over positive phonon wave vectors q. Thus,

$$E_{LA}(t) = \sum_{q>0} \mathcal{E}_{LA}(q,t). \tag{93}$$

The total energy density power spectrum for coherent LA phonons as a function of phonon wave vector q and time is shown in Fig. 16. The peak near $q=0$ is associated with buildup of the steady-state energy density localized in the MQW region. Secondary peaks are seen near $q_0 = 0.59\ \text{nm}^{-1}$ and twice this wave vector, i.e., $q_1 = 2q_0 = 1.18\ \text{nm}^{-1}$. The wave vector q_0 corresponds to the wave vector of the MQW period,

$$q_0 = \frac{2\pi}{L_w + L_b}, \tag{94}$$

where L_w and L_b are the well and barrier widths.

The total coherent LA phonon energy per unit area can be obtained from either Eq. (89) or Eq. (93). In Fig. 17, we show the total phonon energy per unit area, $E_{\text{LA}}(t)$, as a function of time for the coherent LA phonons generated by the driving function shown in Fig. 10. The total energy per unit area is the sum of kinetic- and potential-energy terms. For comparison, the pulse shape is shown as a dotted line. It

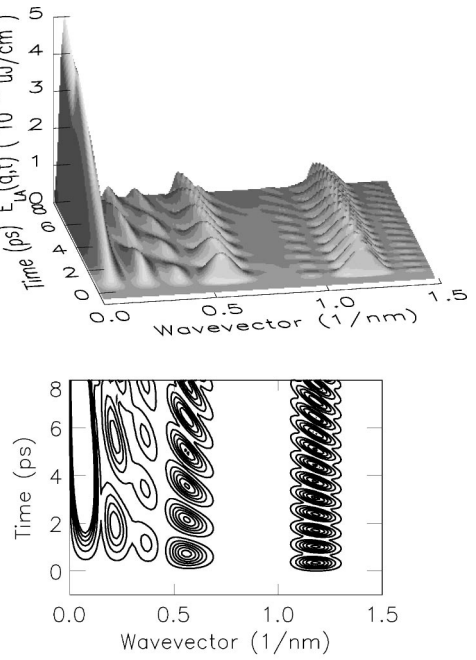

FIG. 16. Total energy density power spectrum $\mathcal{E}_{LA}(q,t)$ for coherent LA phonons as a function of phonon wave vector q and time for the driving function Fig. 10. The total integrated energy density as a function of time is obtained by integrating over q.

is clear from the figure that the buildup of energy in coherent LA phonons takes place on a time scale that is much longer than the pump duration. In addition, we see that the total energy buildup in the phonons saturates at around 5 ps and that some strong but rapidly decreasing oscillations are superimposed on top of an increasing trend.

The saturation phenomenon results from the fact that we have a finite number of quantum wells and not an infinite superlattice. The results can best be explained in terms of the driven string equation. In general, the rate at which energy is fed into the phonon field per unit area is described by the energy equation,[32]

$$\frac{\partial E_{\text{LA}}}{\partial t} = \rho_0 \int_0^L dz S(z,t) V(z,t), \tag{95}$$

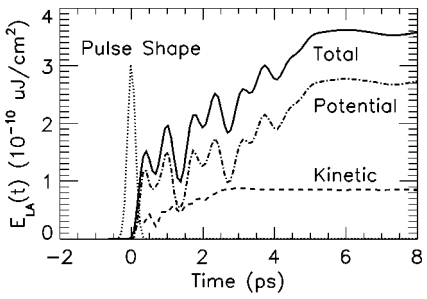

FIG. 17. Integrated energy density $E_{LA}(t)$ as a function of time for coherent LA phonons generated by the driving function shown in Fig. 10. The total integrated energy density is the sum of kinetic- and potential-energy terms. The pulse shape (arbitrary units) is shown for comparison.

in which $S(z,t)$ and $V(z,t)$ are the phonon driving function and velocity fields defined in Eqs. (79) and (56), and ρ_0 is the GaN mass density used for computing the sound speed, C_s, in Eq. (47). The energy equation simply suggests that the rate at which energy is added to a driven string is proportional to the local force times velocity integrated over the length of the string. The integral in Eq. (95) vanishes when the transient velocity field $V(z,t)$ exits the MQW region in which the driving function $S(z,t)$ is localized. Thus, the time, $t_{\rm sat}$, required for $\mathcal{E}_{LA}$ to saturate is just the time it takes for an LA sound wave to cross the MQW, i.e., $t_{\rm sat} \approx W/C_s$, where W is the width of the MQW region over which the driving function is localized. In our example, the LA sound speed is $C_s = 80$ Å/ps in GaN and the MQW width (four-well and three-barrier layers) is $W = 381$ Å, from which we obtain $t_{\rm sat} = 4.8$ ps.

The oscillations of E_{LA} observed in Fig. 17 reflect the number and periodicity of the diode MQW's. The pump laser generates spatially periodic electron and hole distributions, as seen in Fig. 7, due to the fact that the pump photoexcites carriers in the wells but not the barriers. From each of the wells in the MQW, two double-peaked sound pulses emerge traveling in opposite directions thus giving rise to an outwardly propagating velocity field pattern $V(z,t)$ with eight peaks traveling outward in each direction as seen in Fig. 13. The driving function $S(z,t)$, on the other hand, is localized in the MQW's and is relatively constant in time after the pump pulse dies out. The driving functions localized in each well do work on eight traveling velocity disturbances, the two generated in the well itself as well as the ones generated in the three neighboring wells that subsequently pass by. This gives rise to the six peaks plus saturation plateau seen in Fig. 17. The time interval between coresponding peaks in adjacent wells is just the time it takes for the LA sound waves to travel between wells, i.e., $t_{\rm period} = (L_w + L_b)/C_s$, where L_w and L_b are the well and barrier thicknesses. For the MQW structure, $L_w = 63.0$ Å and $L_b = 43.0$ Å and we have $t_{\rm period} = 1.325$ ps, which agrees with the peak-to-peak time between the first and third or second and fourth peaks seen in Fig. 17.

V. SUMMARY AND CONCLUSIONS

We have developed a microscopic theory for the generation and propagation of coherent LA phonons in pseudomorphically strained wurtzite (0001) $In_xGa_{1-x}N/GaN$ multiple quantum well (MQW) *pin* diodes. Both GaN and InN have different lattice constants so that a significant mismatch occurs between the wells and barriers. The presence of strain in the MQW's results in the creation of strain-induced built-in piezoelectric fields on the order of several MV/cm, which significantly alter the electronic and optical properties of the diode structure. In particular, the effective band gap can be lower than the band gap in unstrained $In_xGa_{1-x}N$ wells due to the presence of triangular piezoelectric potentials.

To a first approximation, the generation of coherent LA phonons is driven by optical photoexcitation of electron-hole pairs by an ultrafast Gaussian pump laser. Under typical experimental conditions, the propagation of coherent LA phonons is described by a *uniform* loaded-string equation for the lattice displacement where the time- and position-dependent driving force on the string is a function of the photoexcited carrier density. This differs from coherent LO phonon oscillations in bulk systems where the coherent LO phonons obey a forced oscillator equation. Both deformation potential and piezoelectric coupling mechanisms contribute to the driving force. We find that deformation potential coupling contributes a driving force proportional to the derivative of the carrier density while piezoelectric coupling contributes a driving force proportional to the photoexcited carrier density.

We found that the driving term in the loaded-string equation is suddenly turned on by rapid generation of electron-hole pairs by the pump and remains approximately constant theafter. This sudden displacive loading of the string results in a new static equilibrium lattice displacement. This new static equilibrium displacement corresponds to a population of coherent LA phonons with $q \approx 0$. As the lattice adjusts to the new equilibrium, coherent LA phonons are transmitted in the positive and negative z directions at the LA sound speed. These traveling coherent LA phonons are characterized by $q \approx 2\pi/L$ where L is the superlattice period.

The formalism described here can be applied to the analysis of more complicated device geometries as well as more complicated laser pulse sequences. This gives a simpler method for calculating the coherent LA phonon generation in more complicated geometries and gives additional insight into the acoustic coherent response.

ACKNOWLEDGMENTS

The works of G.D.S. and C.J.S. was supported by the National Science Foundation through Grant No. DMR-9817828 and INT-9414072. The work of C.S.K. was supported by Chonnam National University through a grant in the year 1999.

[1] G.C. Cho, W. Kutt, and H. Kurz, Phys. Rev. Lett. **65**, 764 (1990).
[2] W. Kutt, G.C. Cho, T. Pfeifer, and H. Kurz, Semicond. Sci. Technol. **7**, B77 (1992).
[3] T. Pfeifer, W. Kutt, H. Kurz, and H. Scholz, Phys. Rev. Lett. **69**, 3248 (1992).
[4] T.K. Cheng, J. Vidal, H.J. Zeiger, G. Dresselhaus, M.S. Dresselhaus, and E.P. Ippen, Appl. Phys. Lett. **59**, 1923 (1991).
[5] W. Albricht, T. Kruse, and H. Kurz, Phys. Rev. Lett. **69**, 1451 (1992).
[6] A.V. Kuznetsov and C.J. Stanton, Phys. Rev. Lett. **73**, 3243 (1994).
[7] A.V. Kuznetsov and C.J. Stanton, Phys. Rev. B **51**, 7555 (1995).
[8] E.R. Thoen, G. Steinmeyer, P. Langlois, E.P. Ippen, G.E. Tudry, C.H. Brito Cruz, L.C. Barbosa, and C.L. Sedar, Appl. Phys. Lett.

73, 2149 (1998).
[9] A. Yamamoto, T. Mishina, and Y. Masumoto, Phys. Rev. Lett. **73**, 740 (1994).
[10] A. Bartels, T. Dekorsy, H. Kurz, and K. Köhler, Phys. Rev. Lett. **82**, 1044 (1999).
[11] C.-K. Sun, J.-C. Liang, and X.-Y. Yu, Phys. Rev. Lett. **84**, 179 (2000).
[12] P.Y. Yu and M. Cardona, *Fundamentals of Semiconductors* (Springer-Verlag, Berlin, 1996).
[13] J.B. Jeon, B.C. Lee, M. Sirenko, K.W. Kim, and M.A. Littlejohn, J. Appl. Phys. **82**, 386 (1997).
[14] S.L. Chuang and C.S. Chang, Phys. Rev. B **54**, 2491 (1996).
[15] S.L. Chuang and C.S. Chang, Appl. Phys. Lett. **68**, 1657 (1996).
[16] S.L. Chuang, *Physics of Optoelectronic Devices* (Wiley, New York, 1995).
[17] O. Ambacher, J. Smart, J.R. Shealy, N.G. Weimann, K. Chu, M. Murphy, W.J. Schaff, L.F. Eastman, R. Dimitrov, L. Wittmer, M. Stutzmann, W. Rieger, and J. Hilsenbeck, J. Appl. Phys. **85**, 3222 (1999).
[18] S. Nakamura and G. Fasol, *The Blue Laser Diode: GaN Based Emitters and Lasers*(SpringerVerlag, Berlin, 1997).
[19] Y.C. Yeo, T.C. Chong, and M.F. Li, J. Appl. Phys. **83**, 1429 (1998).
[20] G. Martin, A. Botchkarev, A. Rockett, and H. Morkoç, Appl. Phys. Lett. **68**, 2541 (1996).
[21] B. Doshi, K.F. Brennan, R. Bicknell-Tassius, and F. Grunthaner, Appl. Phys. Lett. **73**, 2784 (1998).
[22] A.F. Wright, J. Appl. Phys. **82**, 2833 (1997).
[23] S.F. Chichibu, A.C. Abare, M.P. Mack, M.S. Minsky, T. Deguchi, D. Cohen, P. Kozodoy, S.B. Fleischer, S. Keller, J.S. Speck, J.E. Bowers, E. Hu, U.K. Mishra, L.A. Coldren, S.P. DenBaars, K. Wada, T. Sota, and S. Nakamura, Mater. Sci. Eng., B **B59**, 298 (1999).
[24] This will affect the forcing term $S(z,t)$ in Eq. (79).
[25] D.L. Smith and C. Mailhiot, J. Appl. Phys. **63**, 2717 (1988).
[26] W. C. Chow, S. W. Koch, and M. Sargent, *Semiconductor-Laser Physics* (Springer-Verlag, Berlin, 1994).
[27] H. Haug and S. W. Koch, *Quantum Theory of the Optical and Electronic Properties of Semiconductors* (World Scientific, Singapore, 1993).
[28] S.H. Park and S.L. Chuang, Phys. Rev. B **59**, 4725 (1999).
[29] J. D. Jackson, *Classical Electrodynamics* (Wiley, New York, 1975).
[30] W. H. Press, S. A. Teukolsky, W. T. Vetterling, and B. P. Flannery, *Numerical Recipes* (Cambridge University Press, New York, 1992).
[31] N.V. Chigarev, D.Yu. Parachuk, X.Y. Pan, and V.E. Gusev, Phys. Rev. B **61**, 15 837 (2000).
[32] P.W. Berg and J. L. McGregor, *Elementary Partial Differential Equations* (Holden-Day, San Francisco, 1966).
[33] B.A. Auld, *Acoustic Fields and Waves in Solids* (Krieger Publishing, Malabar, Florida, 1973).